International Journal of Plasticity 122 (2019) 49–72

Contents lists available at ScienceDirect

International Journal of Plasticity

journal homepage: www.elsevier.com/locate/ijplas

Microstructure evolution of stainless steel subjected to biaxial load path changes: In-situ neutron diffraction and multi-scale modeling

Manas V. Upadhyay[a,1], Jan Capek[b], Tobias Panzner[b], Helena Van Swygenhoven[a,c,*]

[a] Photons for Engineering and Manufacturing, Laboratory for Synchrotron Radiation Condensed Matter, Synchrotron Radiation and Nanotechnology Division, Paul Scherrer Institute, CH-5232, Villigen, PSI, Switzerland

[b] Neutron Imaging and Applied Materials Group, Laboratory for Neutron Scattering and Imaging, Neutrons and Muons Division, Paul Scherrer Institute, CH-5232, Villigen, PSI, Switzerland

[c] Neutrons and X-rays for Mechanics of Materials, IMX, Ecole Polytechnique Federale de Lausanne, CH-1012, Lausanne, Switzerland

ARTICLE INFO

Keywords:
Strain path change
A dislocations
B polycrystalline material
B crystal plasticity
C finite elements

ABSTRACT

The lattice strain and intensity evolution obtained from in-situ neutron diffraction experiments of 316L cruciform samples subjected to 45° and 90° load path changes are presented and predicted using the multi-scale modeling approach proposed in Upadhyay et al., IJP 108 (2018) 144-168. At the macroscale, the multi-scale approach uses the implementation of the viscoplastic self-consistent polycrystalline model as a user-material into ABAQUS finite element framework to predict the non-linearly coupled gauge stresses of the cruciform geometry. The predicted gauge stresses are then used to drive the elasto-viscoplastic fast Fourier transform polycrystalline model to predict the lattice strain and intensity evolutions. Both models use the same dislocation density based hardening law suitable for load path changes. The predicted lattice strain and intensity evolutions match well with the experimental measurements for all reflections studied. The simulation results are analyzed in detail to understand the role of elastic anisotropy, plastic slip, grain neighborhood interactions and cruciform geometry on the microstructural evolution during biaxial load path changes.

1. Introduction

Sheet metals and alloys are often subjected to biaxial loadings and load path changes (LPCs) during their forming processes. Their subsequent mechanical response significantly depends on the multi-axial deformation history. Until recently, however, majority of the research efforts have been dedicated towards understanding the material response, including the Bauschinger effect and change in work hardening, after load reversals from uniaxial tension/compression or shear tests. It is now well accepted that the origin of the macroscopic behavior has to be found at the microstructural level: (a) at the meso-scale or intergranular scale, crystallographic texture evolution and anisotropy play a major role in determining the elastic response, (b) at the microscale or intra-granular level, heterogeneous dislocation activity combined with latent hardening influence the macroscopic hardening behavior (Beyerlein and Tomé, 2007; Christodoulou et al., 1986; Rauch et al., 2007; Takahashi and Shiono, 1991).

In recent years, increased efforts have been dedicated towards understanding the mechanical behavior of materials during biaxial

* Corresponding author. Photons for Engineering and Manufacturing, Laboratory for Synchrotron Radiation Condensed Matter, Synchrotron Radiation and Nanotechnology Division, Paul Scherrer Institute, CH-5232, Villigen, PSI, Switzerland.

E-mail address: helena.vanswygenhoven@psi.ch (H. Van Swygenhoven).

[1] Current address: LMS, C.N.R.S., Ecole Polytechnique, Institut Polytechnique de Paris, 91128 Palaiseau Cedex, France. email: manas.upadhyay@polytechnique.edu.

https://doi.org/10.1016/j.ijplas.2019.06.006
Received 22 August 2018; Received in revised form 2 June 2019; Accepted 7 June 2019
Available online 15 June 2019

loading and LPCs (see (Kuwabara, 2007; Tasan et al., 2012) and references within on different biaxial test setups). Amongst the biaxial testing setups used, the cruciform geometry has the advantage of applying any arbitrary biaxial loading and perform continuous LPC tests. This allows access to a large portion of the 2-dimensional (2D) stress space and LPCs can be performed without changing the test apparatus or re-machining the samples. However, as noted in several works (Bonnand et al., 2011; Hoferlin et al., 1998; MacEwen et al., 1992; Upadhyay et al., 2017b), for most cruciform geometries it is difficult to define the gauge cross-sectional area. This prevents the analytical computation of the gauge stresses. In addition, most cruciform geometries suffer from a non-linear coupling between the in-plane cruciform gauge stress components and the extent of the non-linearity varies according to the type of loading, along with the elastic and plastic material properties (Upadhyay et al., 2017b). While there are some cruciform geometries (Deng et al., 2015; Kuwabara, 2007) that are able to decouple the gauge stresses, they however fail at very low plastic strain making these geometries unsuitable for biaxial LPC tests. Foecke and co-workers (Foecke et al., 2007; Iadicola et al., 2014, 2008) proposed to use the $\sin^2\psi$ x-ray diffraction approach to obtain the gauge stresses during biaxial testing. However, their approach requires making several assumptions on the gauge stress state and obtaining a reliable stress-strain response during LPCs is very time consuming. From a practical standpoint, the most information that can be extracted from a cruciform test setup is the applied forces/displacements in the arms, and the gauge surface strain evolution using techniques such as digital image correlation (DIC).

In a recent work (Upadhyay et al., 2018), we proposed a multi-scale FE approach to predict the gauge stresses during a biaxial LPC test on a cruciform sample. This approach involves using the implementation of the anisotropic viscoplastic self-consistent (VPSC) polycrystalline model (Lebensohn and Tomé, 1993) as a user material subroutine in the ABAQUS/Standard FE framework, i.e. the VPSC-FE model (Patra and Tomé, 2017; Segurado et al., 2012). During a VPSC-FE simulation, each material point in the FE mesh represents a polycrystalline microstructure. The ABAQUS/Standard algorithm invokes the VPSC-FE model to compute the constitutive response (stresses and strains) at each material point while respecting the equilibrium conditions. In (Upadhyay et al., 2018), we implemented a dislocation density based single crystal hardening law suitable for LPCs which was proposed by (Kitayama et al., 2013; Rauch et al., 2011; Wen et al., 2016), in the VPSC-FE model. The combined VPSC-FE model and the hardening law (referred to as the crystallographic-RGBV law after the authors of (Rauch et al., 2011)) was used to simulate the biaxial LPC response of 316L stainless steel cruciform samples. The model was validated by comparing the predicted force vs gauge strains with experimental force vs DIC gauge strain measurements taken during five biaxial LPC experiments on different 316L steel cruciform samples; each sample was first subjected to a uniaxial load-unload cycle followed by biaxial LPCs at different reloading angles in the range $(0°, 90°]$ (Upadhyay et al., 2018). Following validation, the predicted gauge stress evolution was analyzed and polycrystalline yield surfaces were generated to understand the effect of biaxial LPCs on the mechanical response.

The aforementioned biaxial LPC experiments were performed during in-situ neutron diffracton measurements, however in Upadhyay et al. (2018) only the mechanical data were analyzed. In-situ neutron/x-ray diffraction has been widely used to investigate the microstructure evolution during deformation. The changes in the average position, width and intensity of diffraction peaks can be used to extract information on lattice strain, dislocation density and texture evolutions. Combining in-situ diffraction experiments with crystal plasticity modeling can help understand the role of elastic anisotropy, plastic slip and grain neighborhood interactions on the material response. Such synergistic studies have been performed mainly during monotonic loadings (Clausen et al., 1998; Han and Dawson, 2005; Kanjarla et al., 2012; Neil et al., 2010; Oliver et al., 2004; Wang et al., 2013) and LPCs (Chen et al., 2015; Gonzalez et al., 2012; Hu et al., 2016; Marin et al., 2012; Prangnell et al., 1995; Saleh et al., 2013; Wollmershauser et al., 2012) using dog-bone samples; those performed during cruciform biaxial loading and LPCs are recalled. Collins and co-workers performed in-situ x-ray synchrotron diffraction studies during biaxial loading (Collins et al., 2015) and LPCs (Collins et al., 2017) of DX54 steel cruciform samples and combined them with CPFE simulations to understand the lattice strain evolution. Their CPFE simulations used the experimental cruciform gauge strain evolution as boundary conditions. This approach is unable to predict the non-linear coupling between cruciform gauge stresses. The shortcoming was overcome using a multiscale model (Upadhyay et al., 2016, 2017a) that combined (a) a phenomenological elastic-plastic FE model at the macroscale to reliably predict the cruciform gauge stresses during monotonic loading, and (b) the elasto-viscoplastic fast Fourier transform (EVP-FFT) model, originally proposed by Lebensohn et al. [41],to predict the lattice strain evolution. The combined FE-FFT approach was used to predict the lattice strain evolution of a series of in-situ neutron diffraction experiments performed during monotonic biaxial loading (Van Petegem et al., 2016). The hardening laws used in both the models in (Upadhyay et al., 2016) are unable to capture the Bauschinger effect and change in the work hardening response after LPCs. With the modifications to this multi-scale approach proposed in (Upadhyay et al., 2018), i.e. the VPSC-FE and EVP-FFT models implemented with the crystallographic-RGBV hardening law, it is now possible to study the in-situ neutron diffraction results during cruciform biaxial LPCs.

In the aforementioned crystal plasticity and in-situ diffraction studies, the focus has been on comparing and understanding only the lattice strain evolution; changes in peak width and integrated intensity are not studied. Previous attempts at predicting the peak widths have resulted in poor matches with the experimental measurements (Dawson et al., 2005; Kanjarla et al., 2012). The main reason for this mismatch is that most crystal plasticity models simulate the evolution of statistical ensembles of dislocations and do not account for the intragranular stresses arising from lattice distortions due to the presence of dislocations. Recently, Wang et al. (2017) proposed a statistical approach that accounts for intragranular stress distributions from dislocations in crystal plasticity models and predicted peak widths. However, the simulated peak widths needed to be fitted to the measured peak widths to obtain a match. Meanwhile, integrated intensity evolutions have not yet been simulated using crystal plasticity approaches because this requires generating full diffraction peak profiles which is beyond the capabilities of existing crystal plasticity models. However, crystal plasticity models such as the full-field EVP-FFT or CPFE simulate the texture evolution and can predict the change in the number of grains contributing to a diffraction peak. These changes are related to the change in integrated intensity of that peak and therefore can be compared with experimental data.

The main aim of this work is to use the multi-scale modeling approach presented in (Upadhyay et al., 2018), i.e. VPSC-FE and EVP-FFT models implemented with crystallographic-RGBV hardening law, to predict and explain the lattice strain and intensity evolution obtained from in-situ neutron diffraction measurements during biaxial LPC tests of 316L cruciform samples. The paper focusses on two in-situ biaxial LPC tests (a) uniaxial loading and unloading followed by a 45° LPC, and (b) uniaxial loading and unloading followed by a 90° LPC, for which the mechanical response was already presented and analyzed in (Upadhyay et al., 2018).

The article is divided into sections as follows. Section 2 briefly presents the experimental setup and the mechanical response of the two LPC tests performed in (Upadhyay et al., 2018). Section 3 presents the passage of information between the experiments and models, and the simulation setup. Section 4 presents the experimental and simulated lattice strain and intensity evolutions. The discussion in section 5 highlights the role of cruciform geometry, elastic anisotropy, plastic slip, and grain neighborhood effects on the lattice strain and intensity evolution. Section 6 outlines the main conclusions of this study. Theoretical and modeling developments that are necessary for the analysis are presented in the appendix. Additional data supporting the results and discussions in this study are presented as supplementary material.

2. Experiments

2.1. Material and mechanical tests

The as-received material is a warm-rolled sheet of face centered cubic (fcc) 316L stainless steel composed of: Cr-17.25, Ni-12.81, Mo-2.73, Mn-0.86, Si-0.53, C-0.02 (weight %). The sheet is 10.5 mm thick and has in-plane dimensions of 2000 mm × 1000 mm. Electron backscattering diffraction (EBSD) analysis of the as-received 316L sheet revealed a mild texture with an average grain size of 7μm (Van Petegem et al., 2016). Uniaxial deformation along RD and TD showed that the mild texture had a negligible effect on the macroscopic mechanical response and the lattice strain evolutions (Van Petegem et al., 2016). Since here we are also studying the diffraction peak intensity evolutions, which are more sensitive to the underlying texture, the results obtained from crystal plasticity simulations performed using the experimental texture and a random texture are compared in sections 4 and 5.

The cruciform mechanical tests have already been presented in (Upadhyay et al., 2018) and are therefore only briefly recalled here. Cruciform samples are water cut and then mechanically milled to the final geometry shown in Fig. 1a. The manufacturing tolerance for every sample is ±0.05 mm. All samples are prepared such that the RD and TD are respectively aligned along directions 1 and 2. In this work, we focus on two cruciform shaped samples that were subjected to the same first uniaxial load-unload, followed by: (a) a 45° LPC and (b) a 90° LPC.

The cruciform samples were deformed using a biaxial deformation rig having independent arm control (Repper et al., 2013; Van Petegem et al., 2016). The samples are gripped into the machine using bolts that slide into the holes in their arms. To ensure that the samples are properly gripped, they are subjected to an equibiaxial tensile preload of 0.3kN along each arm. All samples are first

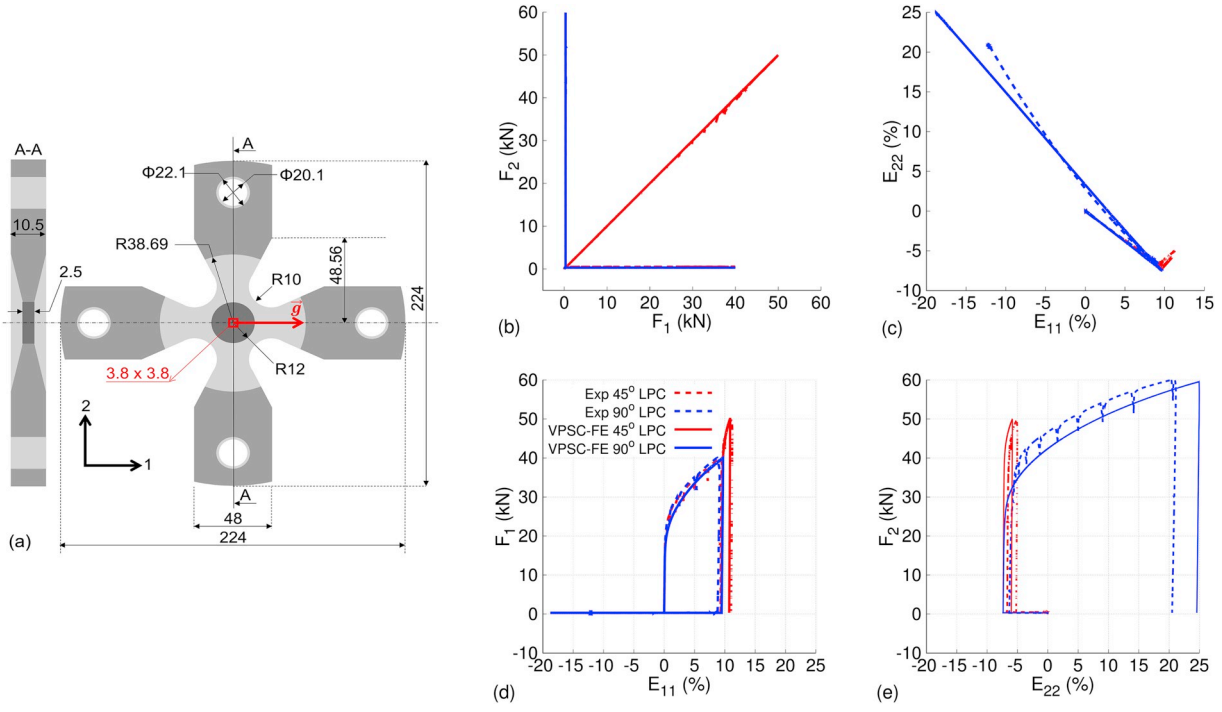

Fig. 1. (a) Cruciform sample geometry used for biaxial LPC tests during in-situ neutron diffraction. The diffraction vector $\vec{\mathbf{g}}$ and the gauge region are highlighted. The experimental and VPSC-FE simulated (b) F_2 vs F_1, (c) E_{22} vs E_{11}, (d) F_1 vs E_{11} and (e) F_2 vs E_{22} curves for the 45° and 90° LPCs. The common legend for (b–e) is shown in (d).

subjected to the same uniaxial tensile first loading along direction 1 to $F_1 = 40$kN and unloaded back to $F_1 = 0.3$kN while F_2 is kept constant at 0.3kN. For the 45° LPC test, the cruciform sample is reloaded under equibiaxial tension to $F_1 = F_2 = 50$kN followed by unloading to $F_1 = F_2 = 0.3$kN. For the 90° LPC, the cruciform sample is loaded to $F_2 = 60$kN followed by an unload to $F_2 = 0.3$kN. For all loadings and unloadings, the force rate along one or both the directions is 80N/s. Fig. 1b shows the F_2 vs F_1 curves for these two LPC tests.

At regular intervals, the loading/unloading is interrupted to collect neutron spectra for 15 minutes. In the elastic regime, the applied forces in the cruciform arms are kept constant during neutron spectra collection. In the plastic regime, the cruciform arms are held at constant displacement to avoid excessive creep of the material. During the initial 5 minutes of each displacement hold, large force relaxations occur in the cruciform arm due to plastic activity in the gauge region. Therefore, in the plastic regime, the measurement begins after an initial wait period of 5 minutes. After neutron spectra collection, the sample is reloaded to the same force levels just before the displacement hold. More details on this loading procedure can be found in (Upadhyay et al., 2018).

In-plane cruciform gauge strain measurements are performed using digital image correlation (DIC). A two-camera ARAMIS4M® DIC system from GOM is installed on the biaxial rig to perform in-situ measurements of surface strains. The macroscopic strains reported in this work are averaged over the gauge area of 3.8×3.8 mm^2 at the center of the cruciform surface shown in Fig. 1a. The averaging procedure is motivated from in-situ neutron diffraction experiments where the diffraction patterns are obtained from the gauge region which is the through thickness volume beneath the 3.8 x 3.8 mm^2 area (Upadhyay et al., 2016, 2017a; Van Petegem et al., 2016). The speckle pattern necessary for DIC measurements is prepared by hand spraying the surface with black and white paint in the sequence: black-white-black. The error associated with the DIC strains is given using the equation: $err(\%) = a$ x strain$(\%) + b$; where a and b are in the range [0.014, 0.024] and [0.05, 0.09], respectively. Fig. 1c, d and e show the E_{22} *vs* E_{11}, F_1 *vs* E_{11} and F_2 *vs* E_{22} curves, respectively, obtained by combining the DIC measurements with the applied forces in cruciform arms for the 45° and 90° LPCs.

2.2. In-situ neutron diffraction

The neutron diffraction experiments are performed at POLDI, a time-of-flight (ToF) thermal neutron diffractometer located at the neutron source SINQ (Paul Scherrer Institute, Switzerland). Details on the POLDI operating principle and setup can be found in (Stuhr, 2005; Stuhr et al., 2005). The incoming beam has a cross-section of 3.8×3.8 mm^2 and it is incident on the central (gauge) region of the circular thinned part of the cruciform samples. A single detector bank is installed at 90° to the incident neutron beam. The detector has an angular acceptance range of $\Delta(2\theta) = \pm 15°$. The neutron diffraction measurements are performed in transmission mode with the biaxial rig and cruciform samples positioned at 45° to the incoming and outgoing beam. This setup ensures that the diffraction vector $\vec{\mathbf{g}}_{\{hkl\}}$ of an $\{hkl\}$ diffraction peak is always parallel to cruciform loading direction 1 as shown in Fig. 1a. An $\{hkl\}$ diffraction peak is obtained when multiple grains having the normal to one of their $\{hkl\}$ planes closely aligned (within ± 7.5°) with $\vec{\mathbf{g}}_{\{hkl\}}$. In this work, the {111}, {200}, {220} and {311} peaks (or grain families) are studied.

The neutron data is analyzed using the POLDI standard single peak fitting procedure implemented in the Mantid software (Arnold et al., 2014). The diffraction peaks are well described using Gaussian functions.

The Mantid software gives the fitted mean position of each $\{hkl\}$ peak related to the mean interplanar spacing $d_{\{hkl\}}$ and the integrated intensity (I_{hkl}) for that $\{hkl\}$ grain family. The relative change in $d_{\{hkl\}}$, with respect to the initial $d^0_{\{hkl\}}$, gives the mean elastic lattice strain $\varepsilon_{\{hkl\}}$ as:

$$\varepsilon^{exp}_{\{hkl\}} = \frac{d_{\{hkl\}} - d^0_{\{hkl\}}}{d^0_{\{hkl\}}} \tag{1}$$

The evolution of $I_{\{hkl\}}$ during plastic deformation is representative of the change in number of grains (texture evolution) of that $\{hkl\}$ grain family contributing to that peak. In this work, we will follow the percentage change in $I_{\{hkl\}}$ with respect to the integrated intensity at the initial state ($I^0_{\{hkl\}}$) for different $\{hkl\}$ peaks:

$$\Delta I^{exp}_{\{hkl\}} = \frac{I_{\{hkl\}} - I^0_{\{hkl\}}}{I^0_{\{hkl\}}} \times 100 \tag{2}$$

3. Simulation setup

The VPSC-FE and EVP-FFT models, implemented with the crystallographic-RGBV hardening law, have already been presented in (Upadhyay et al., 2018). Further details on each of these models can be found in their original works: the VPSC-FE model (Patra and Tomé, 2017; Segurado et al., 2012), the EVP-FFT (Lebensohn et al., 2012), and crystallographic-RGBV hardening law (Kitayama et al., 2013; Rauch et al., 2011; Wen et al., 2016). The governing equations and algorithms of these models relevant to this work have already been presented in (Upadhyay et al., 2018) and are not repeated here.

3.1. Multi-scale passage of information between experiments and models

The multi-scale FE-FFT approach proposed in (Upadhyay et al., 2016, 2017a) to study the cruciform microstructural response during monotonic biaxial loading is extended here to simulate biaxial LPC response. At the macroscale, the phenomenological elasto-

plastic FE model is replaced with the VPSC-FE model implemented with the crystallographic-RGBV hardening law. At the microscale, the same EVP-FFT model is used but now with the crystallographic-RGBV instead of the Voce hardening law. The passage of information between the models and experiments is as follows:

1. The experimental applied forces v/s time curve is used to drive the VPSC-FE simulation.
2. The predicted surface strains from the cruciform gauge area are compared with the DIC results.
3. Following the macroscopic validation,
   a. The VPSC-FE predicted Σ v/s F curves are used to merge with the $\varepsilon^{exp}_{\{hkl\}}$ vs F and $\Delta I^{exp}_{\{hkl\}}$ vs F curves to obtain the $\varepsilon^{exp}_{\{hkl\}}$ vs Σ and the $\Delta I^{exp}_{\{hkl\}}$ vs Σ.
   b. The predicted macroscopic gauge stresses ($\mathbf{\Sigma}$) are used as the macroscopic boundary conditions to drive the EVP-FFT model.
4. The EVP-FFT predicted $\varepsilon^{sim}_{\{hkl\}}$ vs Σ and $\Delta I^{sim}_{\{hkl\}}$ vs Σ evolutions are validated against their experimental counterparts.
5. Following the microscopic validation, the EVP-FFT results are analyzed to understand the microstructural response.

Note that the VPSC-FE simulations used in this work were already performed, presented and validated in (Upadhyay et al., 2018). Therefore, steps 1, 2 and 3a in the above algorithm are not performed in this work.

3.2. Boundary conditions and microstructure

Detailed descriptions for the boundary conditions and simulated microstructure setup can be found in (Upadhyay et al., 2018) for the VPSC-FE model and in (Upadhyay et al., 2018, 2017a, 2016) for the EVP-FFT model. In the following, only the details necessary for this work are briefly recalled.

For the VPSC-FE simulations, only 1/8th part of the cruciform geometry was simulated by imposing appropriate symmetric boundary conditions on cut surfaces. To further improve computational efficiency, the Saint-Venant's principle was invoked to reduce cruciform arms. A structured hexahedron mesh with linear 8-node elements and reduced integration points (C3D8R in ABAQUS) was used. The final FE mesh consists of 1236 elements. For better computational efficiency, a 100-grain random texture was used to perform the VPSC-FE simulations in (Upadhyay et al., 2018); all the VPSC-FE simulations were performed on the Deneb cluster in the high-performance computing facility of the Ecole Polytechnique Fédérale de Lausanne. During the simulations, the applied forces were linearly varied at 80 N/s to the desired experimental values. During post-processing, the gauge strain components are extracted from the central 1.9×1.9 mm^2 surface area of the simulated 1/8th geometry corresponding to the 3.8×3.8 mm^2 area in Fig. 1. The in-plane strain components were averaged over these elements and compared with the corresponding DIC strains. Following validation, simulated gauge stresses were extracted from the 48 through-thickness mesh elements underneath the 1.9×1.9 mm^2 gauge area. These gauge stresses were averaged and their evolution was analyzed. The gauge region is under a biaxial stress state and only the in-plane normal stress components Σ_{11} and Σ_{22} are non-zero. Fig. 2a shows the Σ_{22} vs Σ_{11} curve for first loading and unloading, followed by the 45° LPC and the 90° LPC from the VPSC-FE model obtained from (Upadhyay et al., 2018).

For the EVP-FFT simulations, a synthetic representative microstructure composed of 2500 equiaxed grains was generated. Similar to (Upadhyay et al., 2017a, 2016), the microstructure is divided into 64^3 equi-spaced voxels in 3D space; note that in (Upadhyay et al., 2018), the same microstructure was discretized into 16^3 equi-spaced voxels to facilitate the construction of the polycrystalline yield surfaces.

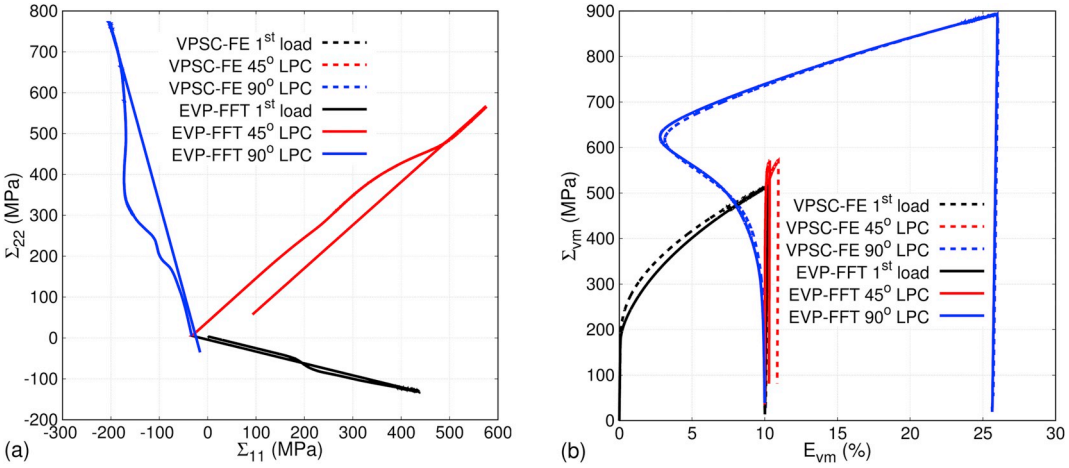

Fig. 2. (a) The in-plane cruciform gauge stresses predicted by the VPSC-FE model and imposed as boundary conditions for the EVP-FFT model for the first loading and unloading, and after the 45° LPC and the 90° LPC. (b) The EVP-FFT fit to the VPSC-FE simulated Σ_{VM} vs E_{VM} curve for the 90° LPC using the hardening law parameters presented in Table 1, and both their predictions for the Σ_{VM} vs E_{VM} curve for the 45° LPC.

3.3. Texture

In accordance with our previous works (Upadhyay et al., 2018, 2017a, 2016), the experimentally measured mild texture of 316L stainless steel is represented by a random texture in the simulations. The VPSC-FE predicted gauge stresses (shown in Fig. 2a) are used as macroscopic boundary conditions to drive the EVP-FFT simulations. Both the 45° LPC and the 90° LPC simulations are performed using this random textured microstructure. As expected, the VPSC-FE and EVP-FFT predicted Σ_{22} vs Σ_{11} curves overlap.

The random texture approximation has thus far worked well for predicting the macroscopic mechanical response and the lattice strain evolutions. However, this may not be the case for the intensity evolution of the diffraction peaks which are more sensitive to the underlying texture. In order to test the influence of the mild texture on the intensity evolution, four additional synthetic microstructures were generated and used to perform EVP-FFT simulations. The four microstructures have the same number of grains, grain morphology and voxelization as the one used for random texture simulations (see section 3.2), but each of these microstructures is assigned a unique set of 2500 crystallographic grain orientations obtained from EBSD measurements. The EVP-FFT simulations for these four experimental texture microstructures are performed only for the 90° LPC.

3.4. Material properties

For all the EVP-FFT simulations presented in this work (except for one in section 5.4), each voxel in the simulated RVE is assigned the anisotropic single crystal elastic properties of 316L stainless steel. Similar to our previous works (Upadhyay et al., 2016, 2017a, 2018), the 3 independent single crystal elastic constants for the fcc 316L stainless steel are taken as: C_{11} = 204.6 GPa, C_{12} = 137.7 GPa and C_{44} = 126.2 GPa (Gonzalez et al., 2012); the Zener anisotropic factor is: $Z = {}^{2C_{44}}/_{(C_{11}-C_{12})} = 3.77$.

VPSC-FE simulations in ABAQUS require inputting the macroscopic elastic stiffness to compute the macroscopic elastic strains at each material point in the FE mesh. To achieve this, the VPSC-FE UMAT interface was implemented with a subroutine that computes the self-consistent estimate of the macroscopic elastic stiffness independently from the VPSC subroutine. Further details on these implementations can be found in (Patra and Tomé, 2017; Segurado et al., 2012; Upadhyay et al., 2018). The self-consistent elastic stiffness is computed using the same single crystal elastic constants as presented above.

In both VPSC-FE and EVP-FFT models, the plastic response of the fcc 316L stainless steel is modeled using the rate-sensitive viscoplastic power law relationship (equation (A6) in (Upadhyay et al., 2018)) between local plastic strain rate and local stress. Dislocation glide is assumed to occur on the 12 {111}<110> slip systems. The viscoplastic power law has two fitting parameters: the reference shear rate $\dot{\gamma}^0$ and the power law exponent n. Usually, $\dot{\gamma}^0$ is arbitrarily assigned and n, which is the inverse rate-sensitivity parameter, is fitted using a stress-strain curve. To avoid fitting n, $\dot{\gamma}^0$ is set to be proportional to the norm of the macroscopic imposed strain rate $|\dot{E}|$ i.e. $\dot{\gamma}^0 = p|\dot{E}|$. Then, the macroscopic response becomes independent of the choice of n, nevertheless, it needs to be assigned to run the simulation. For consistency with previous works (Upadhyay et al., 2018, 2017a, 2016), n is assigned the value 20 and p the value 1.

There are 13 parameters that need to be assigned in the crystallographic-RGBV model; their description is given in Table 1 and appendix A. The parameters D, μ, b, ρ_{min}, ρ_{max}, α^{ss} and $\alpha^{ss'}$ are fixed based on the knowledge of the material and the assumptions made from previous studies that use the crystallographic-RGBV model. The remaining 6 parameters are determined on the basis of the mechanical response obtained from LPC tests. Information on the initial yield point, initial and final hardening rate during the first loading, the yield point after a LPC, the hardening rate during the transient regime after a LPC, and the final hardening rate after a LPC, can be used to determine these parameters.

For the VPSC-FE model, these parameters have already been identified in (Upadhyay et al., 2018) using the shear-reverse shear test and they are listed in Table 1. Using these parameters, the mechanical response of 316L cruciform samples subjected to different biaxial LPCs was predicted and a good match was obtained with the experimental results in (Upadhyay et al., 2018). The VPSC-FE predicted macroscopic force and strain responses for the 45° LPC and 90° LPC are also shown in Fig. 1. As can be seen, the VPSC-FE predicted force vs strain curves correspond to the cusps in the experimental curves caused by the gauge stress relaxations during the displacement holds for collecting neutron spectra (see section 2.3). Note that simulating the stress relaxations would require implementing a creep model such as the one used by Wang and co-workers (Wang et al., 2012, 2013), however this is beyond the scope of the present work.

In (Upadhyay et al., 2018), the same values for the crystallographic-RGBV hardening law parameters were also used for the EVP-FFT simulations to predict yield surfaces. However, since the VPSC-FE and the EVP-FFT frameworks are different, using the same hardening law parameters for both models results in some differences in the final predicted stress-strain response. Therefore, in this work, the crystallographic-RGBV parameters implemented in the EVP-FFT model are calibrated to best fit the VPSC-FE predicted mechanical response at the end of uniaxial first loading and the second loading after the 90° LPC; these fits are also listed in Table 1. This also ensures that the EVP-FFT predicted macroscopic stress vs strain response corresponds to the cusps in the experimental force vs strain curves. Fig. 2b shows the EVP-FFT fit to the VPSC-FE predicted (Upadhyay et al., 2018) von Mises stress $\left(\Sigma_{VM} = \sqrt{\frac{3}{2}\boldsymbol{\Sigma}' : \boldsymbol{\Sigma}'}\right)$ vs von Mises total strain $\left(E_{VM} = \sqrt{\frac{2}{3}\boldsymbol{E}' : \boldsymbol{E}'}\right)$ curve for the 90° LPC, and the predicted Σ_{VM} vs E_{VM} curve for the 45° LPC; $\boldsymbol{\Sigma}'$ and $\boldsymbol{E}'$ are the macroscopic deviatoric Cauchy stress and deviatoric total strain tensors, respectively. The comparison for the 90° LPC test shows a good match between the EVP-FFT and VPSC-FE predictions. When these parameters are also used in the EVP-FFT simulation to predict the E_{VM} during the 45° LPC, the fit is less good. Nevertheless, this should have a negligible effect on the $\varepsilon^{sim}_{\{hkl\}}$ evolution since it depends on the stress state which is correctly captured. Also, for the 45° LPC, the plastic strain increment is very small and therefore will not result in significant changes in intensity.

Note that the VPSC-FE simulations were performed assuming a random texture (Upadhyay et al., 2018) and therefore only the random texture EVP-FFT simulation predicted mechanical response is shown in this figure; nevertheless, the mechanical response predicted by the EVP-FFT simulations performed using the experimental texture also shows a good match with the experimental curve (not shown here).

The CRSS fit for the EVP-FFT model is lower in magnitude from that of the VPSC-FE model. The differences arise from the non-uniqueness of the fitted set of parameters of the crystallographic-RGBV model; this is because the number of unknowns are more than the number of different mechanical test data available. However, within the scope of this paper, this difference shouldn't have any effect on the interpretation of the results.

3.5. Virtual diffraction: lattice strain and change in intensity

The (1,0,0) and (0,1,0) directions of the RVE in EVP-FFT simulations are aligned with the cruciform loading directions 1 ($\vec{\boldsymbol{g}}_{\{hkl\}}$) and 2, respectively. At a given voxel, if an $\{hkl\}$ plane normal defined in the polycrystalline reference frame ($\vec{\boldsymbol{n}}^{poly}_{\{hkl\}}$) is nearly aligned with $\vec{\boldsymbol{g}}_{\{hkl\}}$ then that voxel contributes to the $\{hkl\}$ family. Note that $\vec{\boldsymbol{n}}^{poly}$ is related to the $\{hkl\}$ plane normal in the local crystal frame $\left(\vec{\boldsymbol{n}}^{crys}_{\{hkl\}} = \frac{[hkl]}{||[hkl]||}\right)$ of a voxel as: $\vec{\boldsymbol{n}}^{poly}_{\{hkl\}} = \boldsymbol{R}\cdot\vec{\boldsymbol{n}}^{crys}_{\{hkl\}}$; where $\boldsymbol{R}$ is the transformation (rotation) matrix. In accordance with the neutron diffraction experiment at the POLDI beamline, in the EVP-FFT simulations an $\{hkl\}$ family consists of all voxels whose $\vec{\boldsymbol{n}}^{poly}_{\{hkl\}}$ subtend a solid angle less than or equal to 7.5° with $\vec{\boldsymbol{g}}_{\{hkl\}}$.

The lattice strain at each of these voxels is computed as $\vec{\boldsymbol{g}}_{\{hkl\}}\cdot\boldsymbol{\varepsilon}^{e}\cdot\vec{\boldsymbol{g}}_{\{hkl\}}$. Its average over all voxels contributing to an $\{hkl\}$ family is computed as $\varepsilon^{sim}_{\{hkl\}} = \vec{\boldsymbol{g}}_{\{hkl\}}\cdot\boldsymbol{\varepsilon}^{e}\cdot\vec{\boldsymbol{g}}_{\{hkl\}}$ and compared with the $\varepsilon^{exp}_{\{hkl\}}$ from equation (1).

During plastic deformation, the crystallographic reorientation of voxels (texture evolution) can cause, (i) some voxels that originally contributed to an $\{hkl\}$ family to rotate out such that their $\vec{\boldsymbol{n}}^{poly}_{\{hkl\}}$ subtends a solid angle greater than 7.5° with $\vec{\boldsymbol{g}}_{\{hkl\}}$, and (ii) some voxels that originally did not contribute to an $\{hkl\}$ family to rotate in such that their $\vec{\boldsymbol{n}}^{poly}_{\{hkl\}}$ subtends a solid angle less than or equal to 7.5° with $\vec{\boldsymbol{g}}_{\{hkl\}}$. The percentage change in the number of voxels contributing to an $\{hkl\}$ family, i.e. $\Delta I^{sim}_{\{hkl\}} = \frac{N^{final}_{\{hkl\}} - N^{initial}_{\{hkl\}}}{N^{initial}_{\{hkl\}}} \times 100$, should be related to $\Delta I^{exp}_{\{hkl\}}$ from equation (2).

4. Results

The $\varepsilon^{exp}_{\{hkl\}}$ vs Σ_{VM} and the $\Delta I^{sim}_{\{hkl\}}$ vs E_{VM} evolutions for the 90° LPC obtained from the random texture microstructure are compared with those obtained from the experimental texture microstructure. The comparison is shown in Supplementary Fig. S1. The predicted lattice strain and intensity evolution trends and magnitudes match very well for all the $\{hkl\}$ families, thus justifying the random texture approximation. Henceforth, to be consistent with our previous works (Upadhyay et al., 2018, 2017a, 2016), any reference to the simulated lattice strain and intensity evolutions will be to those obtained from the random textured microstructure simulations, unless mentioned otherwise.

Fig. 3 shows the $\varepsilon^{exp}_{\{hkl\}}$ vs Σ_{VM} and $\varepsilon^{sim}_{\{hkl\}}$ vs Σ_{VM} curves for the {111}, {200}, {220} and {311} families during the 45° LPC and the 90° LPC tests. For all cases, the $\varepsilon^{exp}_{\{hkl\}}$ vs Σ_{VM} curves end at lower Σ_{VM} than their corresponding $\varepsilon^{sim}_{\{hkl\}}$ vs Σ_{VM} curves. These differences occur because the diffraction measurements are performed at the cusps in the force v/s strain curves shown in Fig. 1, and hence there are no diffraction measurements at the maximum force value attained during a given load path. Although the EVP-FFT simulated stress-strain curves fit the hardening response corresponding to these cusps, the simulations are performed up to the stress values that correspond to the maximum applied forces. These result in higher Σ_{VM} values at the end of each load path in the simulation in comparison to the experiments. Fig. 4 shows the $\Delta I^{exp}_{\{hkl\}}$ vs E_{VM} and $\Delta I^{sim}_{\{hkl\}}$ vs E_{VM} curves for the 90° LPC; $\Delta I^{exp}_{\{hkl\}}$ and $\Delta I^{sim}_{\{hkl\}}$ hardly change after the 45° LPC due to small change in plastic strains, and hence they are not shown. The errors in all $\varepsilon^{exp}_{\{hkl\}}$ and $\Delta I^{exp}_{\{hkl\}}$, except for the {220} family, determined by the Mantid software remain low for both LPCs studied. The larger errors for the {220} peaks are because of their low initial intensity (Van Petegem et al., 2016), making it difficult to obtain a reliable measure for $\varepsilon^{exp}_{\{220\}}$. During the first loading, the {220} peak intensity further decreases. Following the 90° LPC, however, the intensity increases by nearly 100%. This increase is sufficient to get a more reliable fit for $\varepsilon^{exp}_{\{220\}}$ but not large enough to get a reliable fit for $\Delta I^{exp}_{\{220\}}$.

In the following, the experimental and simulated lattice strains and intensity evolutions of all $\{hkl\}$ families are analyzed in the following sequence: (1) uniaxial tensile loading and unloading, (2) second loading after a 45° LPC and unloading, and (3) second loading after a 90° LPC and unloading.

4.1. Lattice strain and intensity evolution – uniaxial tensile first loading and unloading

Even though the first loading is the same for both LPC tests, there are some differences observed between their $\varepsilon^{exp}_{\{hkl\}}$, particularly for the {200} family. These differences occur mainly due to the gauge thickness tolerances () between different cruciform samples resulting in different gauge stress magnitudes for the same applied load (Upadhyay et al., 2018). Since the lattice strain magnitudes are dependent on the gauge stress state, the $\varepsilon^{exp}_{\{hkl\}}$ are directly affected by the gauge stress variations between samples.

During the macroscopic elastic regime of the first loading (up to $\Sigma_{VM} \approx 150$ MPa), all the $\varepsilon^{exp}_{\{hkl\}}$ vs Σ_{VM} curves exhibit positive slopes. The same result was obtained in our previous work on monotonic uniaxial cruciform loading (Upadhyay et al., 2016; Van Petegem

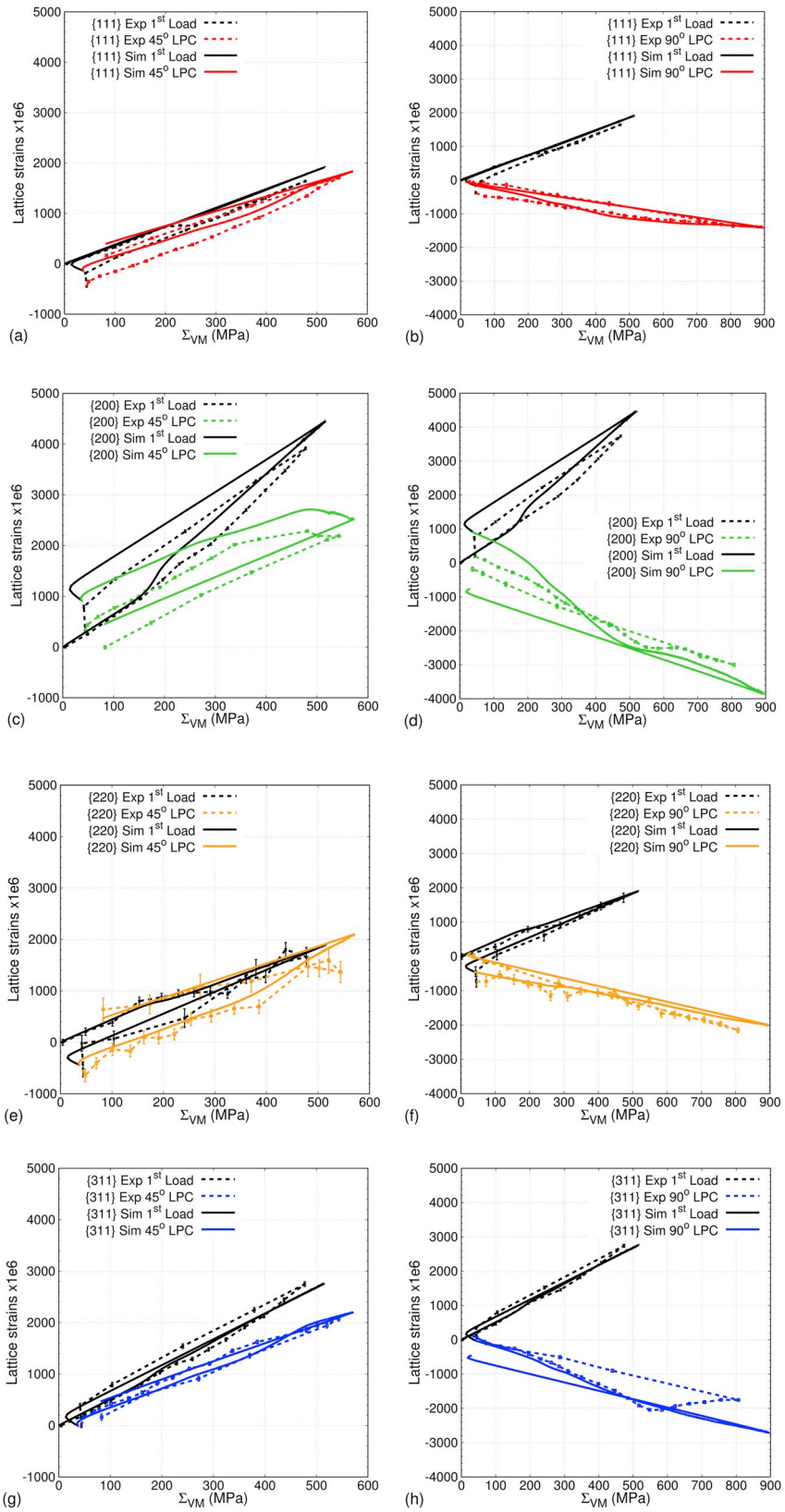

Fig. 3. Comparison between the $\varepsilon^{exp}_{\{hkl\}}$ vs Σ_{VM} and $\varepsilon^{sim}_{\{hkl\}}$ vs Σ_{VM} for the (a, c, e, g) 45° LPC and (b, d, f, h) 90° LPC for the (a, b) {111}, (c, d) {200}, (e, f) {220} and (g, h) {311} families. The first loading and unloading responses are shown in black for both LPCs.

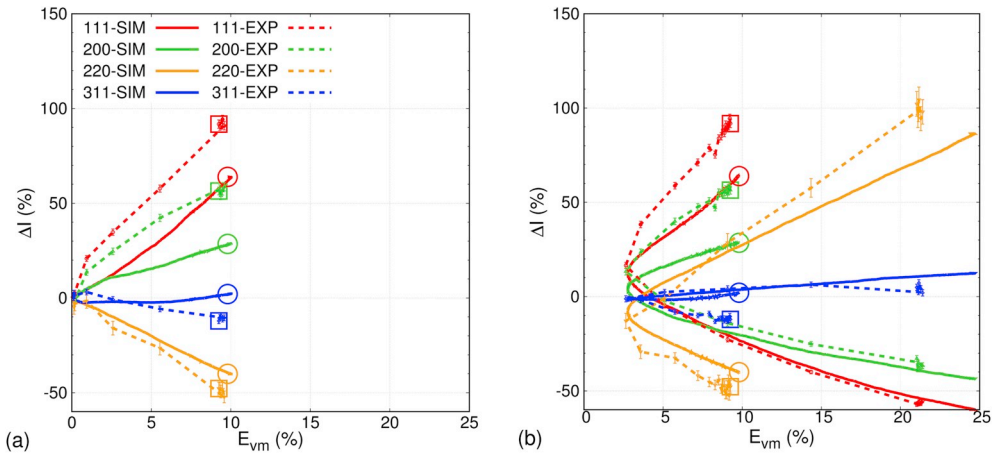

Fig. 4. Comparison between the $\Delta I^{exp}_{\{hkl\}}$ vs E_{VM} and the $\Delta I^{sim}_{\{hkl\}}$ vs E_{VM} evolutions of all $\{hkl\}$ families during the 90° LPC test for (a) the first loading and unloading, and (b) second loading and unloading after the 90° LPC. The colored empty squares and circles in both plots are markers to indicate the end of the first unloading respectively for the $\Delta I^{exp}_{\{hkl\}}$ and $\Delta I^{sim}_{\{hkl\}}$ evolutions. Note that intensity changes are negligible during elastic loading and unloading for any load path. The legends for both plots is shown in (a).

et al., 2016). The positive slopes are a consequence of the increase in $d_{\{hkl\}}$ under the action of the tensile stress Σ_{11} along $\vec{\boldsymbol{g}}$ and compressive stress Σ_{22} normal to $\vec{\boldsymbol{g}}$. Amongst the different $\varepsilon^{exp}_{\{hkl\}}$ vs Σ_{VM}, the {200} family has the most compliant response, the {311} family has an intermediate response, and the {220} and {111} families have nearly equal and stiffest responses. The spread between different $\varepsilon^{exp}_{\{hkl\}}$ vs Σ_{VM} evolutions in this regime is a consequence of the single crystal elastic anisotropy of the material and grain neighborhood interactions (Clausen, 1997; Clausen et al., 1999, 1998). All the $\varepsilon^{sim}_{\{hkl\}}$ vs Σ_{VM} evolutions match very well with their experimental counterparts in this regime.

Since the grains contributing to an $\{hkl\}$ peak remain the same in the elastic regime, $\Delta I^{exp}_{\{hkl\}}$ and $\Delta I^{sim}_{\{hkl\}}$ remain equal to zero in this regime.

Following the on-set of macroscopic plasticity, the slopes of $\varepsilon^{exp}_{\{hkl\}}$ vs Σ_{VM} deviate from their initial linear response because of redistribution of the load carried by different $\{hkl\}$ families due to heterogeneous plastic slip activity. For instance, $\varepsilon^{exp}_{\{200\}}$ and $\varepsilon^{exp}_{\{111\}}$ become respectively more compliant and stiffer, indicating a possible load transfer from the {111} family to the {200} family due to higher plastic activity in the {111} family; note that the load transfer could involve more than two $\{hkl\}$ families. Immediately after the on-set of plasticity, the $\varepsilon^{sim}_{\{hkl\}}$ vs Σ_{VM} curve starts to deviate away from the $\varepsilon^{exp}_{\{hkl\}}$ vs Σ_{VM} response. All $\varepsilon^{sim}_{\{hkl\}}$ vs Σ_{VM} responses exhibit deviations from linearity at lower Σ_{VM} magnitudes than their experimental counterparts. The origin of this can be explained by the earlier yielding of the EVP-FFT fitted Σ_{VM} vs E_{VM} response with respect to the VPSC-FE predicted response in Fig. 2. Additionally, the {111} and {200} families exhibit major differences between their $\varepsilon^{sim}_{\{hkl\}}$ and $\varepsilon^{exp}_{\{hkl\}}$ evolutions. During the elastic-plastic transition, $\varepsilon^{sim}_{\{111\}}$ vs Σ_{VM} evolves nearly linearly in contrast to $\varepsilon^{exp}_{\{111\}}$ vs Σ_{VM}. Furthermore, $\varepsilon^{sim}_{\{200\}}$ vs Σ_{VM} evolves non-linearly in contrast to $\varepsilon^{exp}_{\{200\}}$ vs Σ_{VM}. The $\varepsilon^{sim}_{\{220\}}$ vs Σ_{VM} and the $\varepsilon^{sim}_{\{311\}}$ vs Σ_{VM} evolutions exhibit trends similar to their experimental counterparts.

All the $\Delta I^{exp}_{\{hkl\}}$ vs E_{VM} evolve similar to those reported in (Van Petegem et al., 2016), i.e. the intensity increases for the {111} and {200} families, remains nearly the same for the {311} family, and decreases for the {220} family. The changes in intensity reflect the changes in texture due to grain rotations caused by plastic slip. All $\Delta I^{sim}_{\{hkl\}}$ vs E_{VM} evolutions exhibit similar trends as observed in the experiments. However, the magnitudes of $\Delta I^{sim}_{\{111\}}$ and $\Delta I^{sim}_{\{200\}}$ differ significantly from the experimental ones. The origin of these differences are discussed in section 5.

During the unloading, all $\varepsilon^{exp}_{\{hkl\}}$ and $\varepsilon^{sim}_{\{hkl\}}$ evolve linearly with respect to Σ_{VM}. Towards the end of the unloading, both evolutions become non-linear. This can be explained as follows: towards the end of the first unloading, the cruciform gauge stresses change from the 4th quadrant to the 2nd quadrant in the 2-dimensional (2D) stress space (see Fig. 2a); while both $\varepsilon^{exp}_{\{hkl\}}$ and $\varepsilon^{sim}_{\{hkl\}}$ are decreasing, Σ_{VM} decreases in the 4th quadrant and increases in the 2nd quadrant. At the unloaded state, the $\varepsilon^{exp}_{\{hkl\}}$ values indicate that the {111} and {220} families are under compression, and the {200} and {311} families are slightly under tension.

As can be expected, none of the $\Delta I^{exp}_{\{hkl\}}$ and $\Delta I^{sim}_{\{hkl\}}$ evolve during the elastic unloading.

4.2. Lattice strain and intensity evolution – after 45° LPC

In the macroscopic elastic regime after the 45° LPC, all the $\varepsilon^{exp}_{\{hkl\}}$ vs Σ_{VM} curves have again positive slopes. With respect to the first loading, the $\varepsilon^{exp}_{\{111\}}$ vs Σ_{VM} and $\varepsilon^{exp}_{\{220\}}$ vs Σ_{VM} curves have similar slopes whereas both $\varepsilon^{exp}_{\{200\}}$ vs Σ_{VM} and $\varepsilon^{exp}_{\{311\}}$ vs Σ_{VM} curves exhibit a stiffer response. Insights on these differences can be obtained by comparing the evolutions with those during monotonic uniaxial tension and monotonic equibiaxial tension without preloads from (Upadhyay et al., 2016; Van Petegem et al., 2016). Under monotonic uniaxial tension, $\varepsilon^{exp}_{\{hkl\}} = \frac{1}{E_{\{hkl\}}}\Sigma_{11}$ whereas under monotonic equibiaxial tension $\varepsilon^{exp}_{\{hkl\}} = \frac{1-\nu_{\{hkl\}}}{E_{\{hkl\}}}\Sigma_{11}$; where $E_{\{hkl\}}$ and $\nu_{\{hkl\}}$ are the Young's modulus and Poisson's ratio for the $\{hkl\}$ family, respectively. Therefore, for the same Σ_{11}, monotonic equibiaxial tension results in a

stiffer $\varepsilon^{exp}_{\{hkl\}}$ response. The same trend is followed in the macroscopic elastic regime after a 45° LPC. Following the onset of macroscopic plasticity, $\varepsilon^{exp}_{\{200\}}$ begins to decrease in magnitude with increasing Σ_{VM} implying that the {200} family is shedding its tensile load. The deviation from linearity is significant in comparison to the $\varepsilon^{exp}_{\{200\}}$ vs Σ_{VM} evolution during monotonic equibiaxial tensile loading shown in (Van Petegem et al., 2016). All the $\varepsilon^{sim}_{\{hkl\}}$ vs Σ_{VM} curves match well with the experimental curves.

Due to small changes in E_{VM} after the 45° LPC, there are no significant changes in $\Delta I^{exp}_{\{hkl\}}$ and $\Delta I^{sim}_{\{hkl\}}$.

4.3. Lattice strain and intensity evolution – after 90° LPC

Immediately after the 90° LPC, the macroscopic stress vector subtends an angle higher than 90° with respect to direction 1 (and $\vec{g}$) in the 2D stress space. Consequently, $d_{\{hkl\}}$ of the {*hkl*} grains (with plane normal aligned to $\vec{g}$) decreases with respect to $d^0_{\{hkl\}}$, thus resulting in negative $\varepsilon^{exp}_{\{hkl\}}$ for all {*hkl*} families. Similar to the first load, $\varepsilon^{exp}_{\{200\}}$ vs Σ_{VM} and $\varepsilon^{exp}_{\{111\}}$ vs Σ_{VM} respectively have the most complaint and stiffest responses. Following the onset of macroscopic plasticity during the second load, $\varepsilon^{exp}_{\{220\}}$ vs Σ_{VM} continues to evolve nearly linearly whereas $\varepsilon^{exp}_{\{111\}}$ vs Σ_{VM}, $\varepsilon^{exp}_{\{200\}}$ vs Σ_{VM} and $\varepsilon^{exp}_{\{311\}}$ vs Σ_{VM} exhibit deviations from linearity. $\varepsilon^{exp}_{\{111\}}$ vs Σ_{VM} evolution has one point of inflection and then a nearly constant negative slope suggesting no further change in the proportion of the applied load carried by the {111} family. However, three distinct inflection points are encountered in the $\varepsilon^{exp}_{\{200\}}$ vs Σ_{VM} evolution implying a complex back-and-forth load exchange with other {*hkl*} families. The final slope of the $\varepsilon^{exp}_{\{200\}}$ vs Σ_{VM} curve is also nearly constant. Meanwhile, $\varepsilon^{exp}_{\{311\}}$ starts evolving with a positive slope implying that this family is shedding its compressive load.

The $\varepsilon^{sim}_{\{220\}}$ vs Σ_{VM} match well with the $\varepsilon^{exp}_{\{220\}}$ vs Σ_{VM} (within the experimental errors) also after the 90° LPC. For the {111} and {200} families, the differences between the $\varepsilon^{sim}_{\{hkl\}}$ vs Σ_{VM} and the $\varepsilon^{exp}_{\{hkl\}}$ vs Σ_{VM} decrease during the macroscopic elastic regime of the second loading and simulations predict well the experimental evolutions in the plastic regime. Meanwhile, the $\varepsilon^{sim}_{\{311\}}$ vs Σ_{VM} evolution matches well with the experiments until the end of the macroscopic elastic-plastic transition regime. Hereafter, however, significant differences are observed. The origin of these differences will be explained in section 5.

The $\Delta I^{exp}_{\{hkl\}}$ vs E_{VM} evolution after the 90° LPC inverses with respect to the first loading i.e. the $\Delta I^{exp}_{\{111\}}$ and $\Delta I^{exp}_{\{200\}}$ significantly decrease, $\Delta I^{exp}_{\{311\}}$ slightly increases, and $\Delta I^{exp}_{\{220\}}$ significantly increases. Note that during the second loading, E_{VM} initially decreases and then increases with increasing load. During the decrease in E_{VM}, all $\Delta I^{exp}_{\{hkl\}}$ vs E_{VM} curves have nearly the same slope as during the first loading.

Interestingly, following the 90° LPC, the differences between the experimental and simulated intensity evolutions for the {111}, {200} and {311} families reduce and towards the end of the second load they match very well. Meanwhile, the differences increase slightly between the experimental and simulated intensity of the {220} family, nevertheless, the experimental trends are well captured.

5. Discussion

The simulation results shown in section capture well the experimental lattice strain and intensity evolutions of different {*hkl*} families during 45° LPC and 90° LPC. There are however also some differences. In what follows, the simulated microstructural response is analyzed in detail to understand the origin of these differences as well as the role of elastic anisotropy, plastic slip, grain neighborhood effects and the macroscopic stress state influenced by the cruciform geometry on the microstructural response. The focus will be on answering the following questions:

1) Why do the simulated changes in intensity of the {111} and {200} families differ significantly from the experimental evolutions during the first loading?
2) What is the origin of the difference between the experimental and simulated lattice strain evolution of the {311} family in the macroscopic plastic regime after the 90° LPC?
3) Why is the intensity of the {311} family not evolving during plastic deformation, whereas significant changes are observed in the intensities of all other families during the entire 90° LPC test?
4) What is the role of elastic anisotropy, plastic slip and grain neighborhood on the lattice strain evolution?
5) What is the role of elastic anisotropy and grain neighborhood on the intensity evolutions?
6) What is the role of the cruciform geometry induced non-linear gauge stress response on the lattice strain evolution during the 90° LPC test in comparison with a 90° LPC test performed using dog-bone samples (Zaman et al., 2018)?

To answer these questions and understand the microstructural response, we divide the {*hkl*} families into subsets, as done in previous works (Upadhyay et al., 2016, 2017a). In the rest of this article, only the simulation results from the random texture microstructure will be analyzed and the superscript ‘ *sim*’ will no longer be used.

5.1. Dividing {*hkl*} families into subsets

All grains in an {*hkl*} family have the loading direction 1 (and $\vec{g}$) normal to one of their {*hkl*} planes and the loading direction 2 contained in that plane (and perpendicular to $\vec{g}$). Every {*hkl*} family can be divided into subsets based on these two loading directions. If $<a_i b_i c_i>$ is the set of all possible directions contained in an {*hkl*} plane, then we define an {*hkl*} subset as $\{hkl\}<a_i b_i c_i>$. The

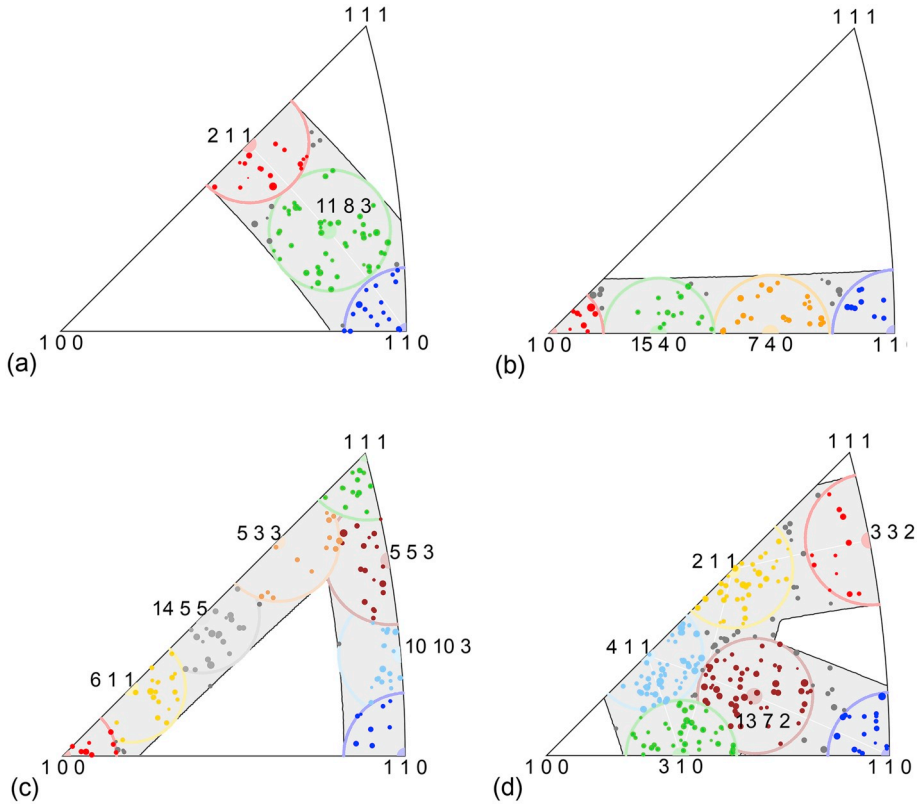

Fig. 5. Inverse pole figures (IPFs) showing in grey the range of all possible subsets of the (a) {111}, (b) {200}, (c) {220} and (d) {311} families as seen along direction 2 of the cruciform sample with an angular range of ± 7.5°. The $a_i b_i c_i$ indices of each subset are marked at their appropriate position, translucent filled circles, in the IPF of their respective {*hkl*} families. These positions form the centroids of the IPF regions bounded by the colored arcs. The size of a bounded region determines the number of grains belonging to its associated subset also within an angular range of ± 7.5° with respect to direction 2. The colored solid dots in each IPF are representative of individual grains from the initial simulated microstructure. The dots are colored according to the subsets to which they belong. The position of each dot is determined by the initial average grain orientation and its size is determined by the number of voxels belonging to the associated grain. In each {*hkl*} IPF, the dark grey dots represent the grains that belong to that {*hkl*} family but not to any of its subsets studied here.

procedure to choose these {*hkl*}<$a_i b_i c_i$> subsets is described in detail in Appendix B. Fig. 5 shows the inverse pole figure (IPF) plots highlighting (in grey) the region where all possible {*hkl*}<$a_i b_i c_i$> subsets for the four {*hkl*} families can be found while looking along direction 2 with an angular tolerance of ± 7.5°. Unlike the grain family subdivision techniques used in other works (Clausen, 1997; Clausen et al., 1999; Upadhyay et al., 2016, 2017a), the proposed subdivision maps a significantly larger portion of all the {*hkl*} grains

Table 1
Crystallographic-RGBV hardening law parameters used for the VPSC-FE simulations performed in (Upadhyay et al., 2018), and for the EVP-FFT simulations in this work.

crystallographic-RGBV hardening law parameters	VPSC-FE	EVP-FFT
τ_0^s (Initial CRSS per slip system in MPa)	123	48
μ (Shear modulus in GPa)	85	85
b (Burgers vector in A^o)	2.5243	2.5243
$\alpha^{ss'}$ (Interaction matrix) ($s = s'$)	0.2	0.2
($s \neq s'$)	0.45	0.45
ρ_{min} (Lower reversibility threshold in m^{-2})	10^{11}	10^{11}
ρ_{max} (Upper reversibility threshold in m^{-2})	10^{14}	10^{15}
f (Recovery parameter)	1	0.8
m (Recombination rate parameter)	14	5.5
K (Mobile to storage parameter)	158	900
D (Grain size in μm)	7	7
f_B^s (back-stress parameter)	0.5	0.4
q (back-stress parameter)	12	4.4

Table 2
The list of {*hkl*} families and their {*hkl*}<$a_i b_i c_i$> subsets studied in this work, along with their multiplicity and the number of voxels in the simulated initial microstructure.

{*hkl*} family	{*hkl*}multiplicity	# of voxels	{*hkl*}<$a_i b_i c_i$> subsets	{*hkl*}<$a_i b_i c_i$> multiplicity	# of voxels
{111}	8	9236	{111}<2 1 1>	6	1621
			{111}<11 8 3>	12	5029
			{111}<1 1 0>	6	1604
{200}	6	7104	{200}<1 0 0>	4	989
			{200}<15 4 0>	8	1436
			{200}<7 4 0>	8	2377
			{200}<1 1 0>	4	1062
{220}	12	13240	{220}<1 0 0>	2	904
			{220}<6 1 1>	4	1828
			{220}<14 5 5>	4	2588
			{220}<5 3 3>	4	1202
			{220}<5 5 3>	4	1642
			{220}<1 1 1>	4	1356
			{220}<10 10 3>	4	1767
			{220}<1 1 0>	2	755
{311}	24	26627	{311}<2 3 3>	2	1071
			{311}<2 1 1>	4	3977
			{311}<4 1 1>	4	3509
			{311}<3 1 0>	4	3655
			{311}<13 7 2>	4	3580
			{311}<1 1 0>	2	1844

(or voxels). Table 2 shows the number of voxels for each {*hkl*} family and their subsets at the initial state of the simulated RVE. In a randomly textured microstructure with equiaxed grains, the number of voxels contributing to an {*hkl*} family are determined by their multiplicity; the higher the {*hkl*} multiplicity factor the more voxels or grains belong to that family as can be seen in Table 2. The subsets of the {111}, {200}, {220} and {311} families capture 89.4%, 82.5%, 91% and 66%, respectively, of all the voxels belonging to these families. The number of voxels belonging to an {*hkl*}<$a_i b_i c_i$> subset are determined by the number of voxels belonging to an {*hkl*} family and the multiplicity of the {*hkl*}<$a_i b_i c_i$> subset. Note that the multiplicity of each {*hkl*}<$a_i b_i c_i$> subset is defined with respect to its {*hkl*} family and it is determined using all 6 indices identifying that subset. Table 2 also shows the multiplicity of each {*hkl*}<$a_i b_i c_i$> subset and the number of voxels belonging to them. In some cases, {*hkl*}<$a_i b_i c_i$> subsets belonging to the same {*hkl*} family and having the same multiplicities, have a large difference in their number of voxels. This difference occurs because the simulated microstructure doesn't have sufficient number of voxels (or grains) to correctly respect the multiplicity of each {*hkl*}<$a_i b_i c_i$> subset. Increasing the number of voxels in the simulated microstructure can solve this problem. However, since there is no experimental information available on the number of grains contributing to each {*hkl*} family or its subsets, such a simulation cannot contribute to further validation. Nevertheless, qualitative inferences can be drawn using the current simulated microstructure.

In what follows, the $\varepsilon_{\{hkl\}<a_i b_i c_i>}$ and $\Delta I_{\{hkl\}<a_i b_i c_i>}$ evolutions are analyzed in detail for the 90° LPC. The same approach can also be used to analyze these quantities for the 45° LPC but this will not be performed here.

5.2. Lattice strain and intensity evolution of the {**hkl**}<$\mathbf{a_i b_i c_i}$> subsets for 90° LPC test

Fig. 6 shows the lattice strains $\varepsilon_{\{hkl\}<a_i b_i c_i>}$ for all {*hkl*} families along with the simulated average $\varepsilon_{\{hkl\}}$ and measured $\varepsilon^{exp}_{\{hkl\}}$ for the 90° LPC test. For each {*hkl*} family, the $\varepsilon_{\{hkl\}<a_i b_i c_i>}$ are following the experimental trends well, proving the robustness of the subdivision technique used. In the elastic regime of the first load, $\varepsilon_{\{111\}<a_i b_i c_i>}$, $\varepsilon_{\{200\}<a_i b_i c_i>}$ and $\varepsilon_{\{311\}<a_i b_i c_i>}$ evolve nearly similar to their respective $\varepsilon_{\{hkl\}}$ (black curve) whereas small divergences are observed for $\varepsilon_{\{220\}<a_i b_i c_i>}$. This implies that in the elastic regime of the first load, the elastic anisotropy and local grain neighborhood have a similar effect on the lattice strain evolution of the subsets within each of the {111}, {200} and {311} families, but they affect each {220}<$a_i b_i c_i$> subset differently. Following the onset of macroscopic plasticity, all the $\varepsilon_{\{111\}<a_i b_i c_i>}$ and $\varepsilon_{\{200\}<a_i b_i c_i>}$ continue to follow their respective $\varepsilon_{\{hkl\}}$ evolutions whereas $\varepsilon_{\{220\}<a_i b_i c_i>}$ and $\varepsilon_{\{311\}<a_i b_i c_i>}$ deviate away. The similarities and differences in the magnitudes of these $\varepsilon_{\{hkl\}<a_i b_i c_i>}$ remain constant during the first unloading. During the second loading, the $\varepsilon_{\{hkl\}<a_i b_i c_i>}$ begin to evolve non-linearly immediately following the 90° LPC. Note here that even though it is possible to discern a macroscopic elastic regime for the second loading (see Fig. 2), this is not evident at the microstructural level due to the non-linear evolution of nearly all $\varepsilon_{\{hkl\}<a_i b_i c_i>}$ immediately after the LPC. In other words, the effect of localized plasticity is more evident at the microstructural scale than at the macroscopic scale. Following the onset of macroscopic plasticity, all {*hkl*} families exhibit a spread in their respective $\varepsilon_{\{hkl\}<a_i b_i c_i>}$. The spread in $\varepsilon_{\{hkl\}<a_i b_i c_i>}$ is much larger for the {200}, {220} and {311} families than for the {111} family.

Fig. 7 shows the percentage change in intensity $\Delta I_{\{hkl\}<a_i b_i c_i>}$ vs E_{VM} evolution for the {111}<$a_i b_i c_i$> and the {311}<$a_i b_i c_i$> subsets; the $\Delta I_{\{200\}<a_i b_i c_i>}$ vs E_{VM} and $\Delta I_{\{220\}<a_i b_i c_i>}$ vs E_{VM} evolutions are shown in Supplementary Fig. S2. During the first loading, the calculated intensity increase of the {111}<2 1 1> subset is higher than that calculated for the entire {111} family (black curve) and

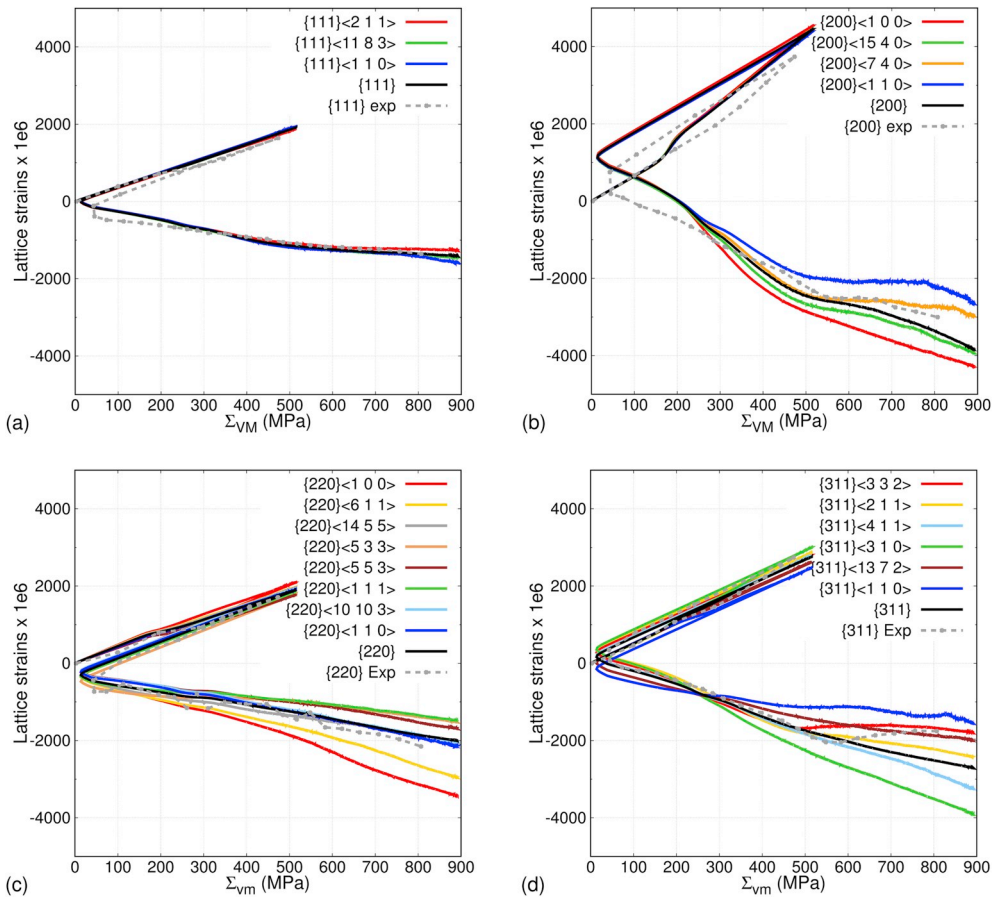

Fig. 6. Comparison between the evolutions of $\varepsilon^{exp}_{\{hkl\}}$, $\varepsilon_{\{hkl\}}$ and $\varepsilon_{\{hkl\}<a_ib_ic_i>}$ as a function of Σ_{VM} for the (a) {111}, (b) {200}, (c) {220} and (d) {311} families during the 90° LPC simulation; for clarity, the second unloading is not shown.

increases beyond the experimental magnitude towards the end of LP1; the change in intensities of the {111}<1 1 0> and {111}<11 8 3> subsets remain, respectively, similar and lower than the experimental magnitude. However, as seen from Table 2, the number of voxels (or grains) belonging to the {111}<2 1 1> subset occupy a small volume fraction of the total number of voxels contributing to the entire {111} family. In fact, the number of voxels belonging to the {111}<11 8 3> subset significantly outnumber the number of voxels of the other two {111}<$a_ib_ic_i$> subsets during the first loading. Since the computed change in intensity of the {111} grain family can be considered as a weighted average of the computed intensities of its subsets, this results in the observed difference between $\Delta I^{exp}_{\{111\}}$ and $\Delta I_{\{111\}}$ during the first loading. The same analogy can be applied to explain the differences between $\Delta I_{\{200\}}$ and $\Delta I^{exp}_{\{200\}}$.

The differences between calculated and experimental intensities could arise from differences in simulated texture, grain morphology and neighborhoods of the {hkl}<$a_ib_ic_i$> subsets. In this work, we simulate a random-textured microstructure with equiaxed grains that is representative of the initial texture and morphology of the 316L stainless steel derived from 2D EBSD measurements (Van Petegem et al., 2016). However, the proportion of grains belonging to the {hkl}<$a_ib_ic_i$> subsets and their precise morphology cannot be easily obtained from EBSD measurements. Furthermore, the simulated grain neighborhoods are not representative of the experimental microstructure. All these discrepancies together could be at the origin of the significant differences between the $\Delta I_{\{hkl\}}$ and $\Delta I^{exp}_{\{hkl\}}$ for the {111} and {200} families. These differences are expected to reduce when the EVP-FFT simulations are performed using fully 3D microstructural input obtained by advanced characterization methods. The above discussion answers question #1.

After the 90° LPC, the $\Delta I_{\{111\}<11\ 8\ 3>}$ evolution is much closer to the $\Delta I^{exp}_{\{111\}}$ evolution. Furthermore, even though at the end of the second loading the number of voxels of the {111}<11 8 3> subset decrease by more than 50% of their initial value, they are sufficiently larger than those of the other subsets and therefore bring the $\Delta I_{\{111\}}$ evolution closer to the $\Delta I^{exp}_{\{111\}}$. The same analogy can be applied to explain the similarities between the $\Delta I^{exp}_{\{hkl\}}$ and $\Delta I^{sim}_{\{hkl\}}$ of the other {hkl} families.

Focusing on the {311} family, even though the average $\Delta I_{\{311\}}$ remains nearly unchanged, there are relatively large changes in $\Delta I_{\{311\}<a_ib_ic_i>}$ during the first loading which become even more pronounced after the 90° LPC. At the end of the second loading, the number of voxels contributing to the {311}<3 3 2> subset increases by more than 300%. However, from Table 2 it can be seen that only ~ 12% of all the voxels contributing to the {311} family are contributing to this subset at the end of the loading. The contribution to $\varepsilon_{\{311\}}$ from the remaining voxels significantly outweighs the contribution of the {311}<3 3 2> subset. Consequently, at the end of the

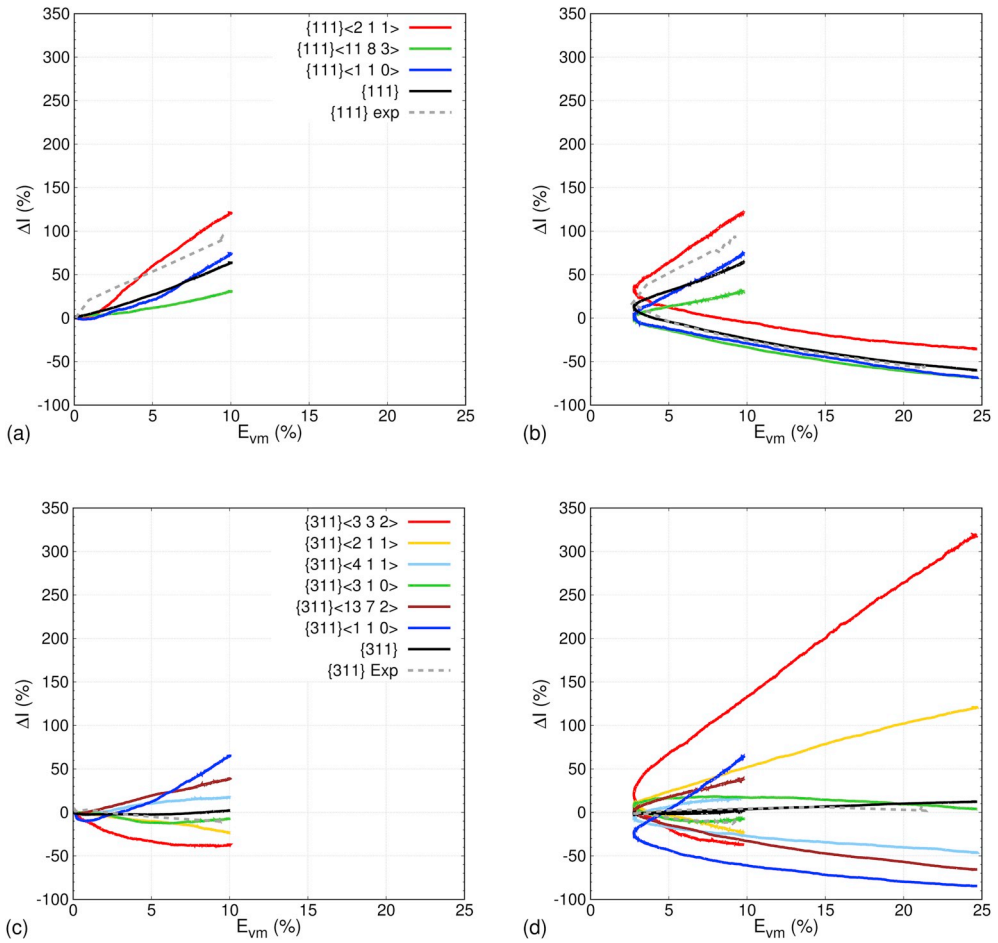

Fig. 7. The $\Delta I^{exp}_{\{hkl\}}$, $\Delta I_{\{hkl\}}$, and $\Delta I_{\{hkl\}<a_i b_i c_i>}$ evolutions as a function of E_{VM} for the (a, b) {111} and (c, d) {311} families during (a, c) the first loading and unloading, and (b, d) the second loading and unloading after a 90° LPC. The legends for (b) and (d) are shown in (a) and (c), respectively.

second load, even though the $\varepsilon_{\{311\}<3\,3\,2>}$ vs Σ_{VM} evolution matches well with the $\varepsilon^{exp}_{\{311\}}$ vs Σ_{VM} evolution, the average $\varepsilon_{\{311\}}$ vs Σ_{VM} evolution has a poor match. This answers question #2.

Next, we focus on the evolution of the absolute number of voxels (proportional to number of grains) contributing to the {311} family for the 90° LPC which will allow to answer question #3. At the initial state, there are 26627 voxels (249 grains) contributing to the {311} family. At the end of the first and the second loadings, these become 27066 and 30145 voxels (257 and 288 grains), respectively. While the changes in the number of voxels at the initial state and at the end of first or second loading may not be large, there are significant changes in the set of grains contributing to this peak. At the end of first loading, although the total number of voxels contributing to the {311} family has only increased by 439, there are 8525 and 8086 voxels (55 and 47 grains) that have respectively rotated in and out of this family. These numbers significantly increase at the end of second loading where 22908 and 19829 voxels (173 and 142 grains) have rotated in and out, respectively. At the end of the first and second loadings, respectively, 69.6% and 36.8% of the initial voxels continue contributing to the {311} family. These results give an insight on how the plastic deformation occurring during the first and second loadings results in significant changes in the set of voxels (grains) contributing to the {311} family and yet the net change is relatively small, explaining why the intensity of this family hardly changes (question #3).

One can go a step further and visualize the direction in which grains rotate in or out of the {311} family using an IPF as shown in Fig. 8 (viewed along cruciform direction 1). During the first loading, on average the outgoing grains rotate towards the {200} and {211} families whereas the incoming grains are rotating in from the {210} family. The average trend in incoming and outgoing voxels (grains) reverses during the second loading. Furthermore, during the first loading, majority of the grains moving in or out of the {311} family lie very close to the yellow arc demarking the IPF region belonging to the {311} family. During the second loading however, grains further away from this arc begin to rotate in or out of the {311} family. These results imply that (i) as the E_{VM} increases, the grains that are increasingly further away from the edge of the detector range (yellow arc in Fig. 8) begin to move in or out of the {311} family, and (ii) the direction of this movement reverses after a 90° LPC. Fig. 8 confirms that the net change in the number of grains contributing to the {311} family is relatively small.

At the beginning of section 4, it was reported that the $\varepsilon^{sim}_{\{hkl\}}$ vs Σ_{VM} and $\Delta I^{sim}_{\{hkl\}}$ vs E_{VM} evolutions obtained from the random texture

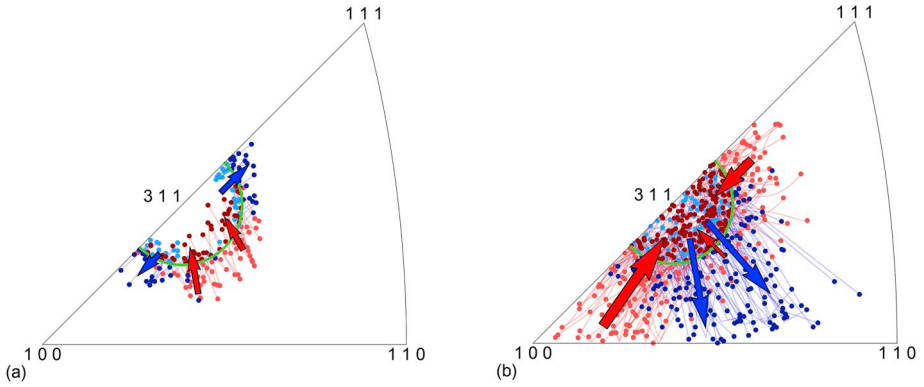

Fig. 8. IPFs of the {311} family showing the movement of grains in and out of the {311} family during (a) the first loading and (b) the second loading of the 90° LPC. The yellow arc demarcates the region of the IPFs belonging to the {311} family when viewed along direction 1. The dots represent only those grains that are moving in or out of the {311} family during deformation and the position of these dots is determined by the average grain orientation. For both loadings, the lighter red dots represent grains that rotate into the {311} family and turn into darker red dots. The lighter blue dots represent {311} grains that rotate out of this family and become darker blue dots at the end of that loading. The lines connecting these dots show the trajectory of the orientation changes in the grains. The arrows represent the average direction followed by the grains moving in or out of the {311} family. (For interpretation of the references to color in this figure legend, the reader is referred to the Web version of this article.)

simulation are similar to those obtained from the experimental texture simulations. This comparison also needs to be performed for the $\{hkl\}<a_ib_ic_i>$ subsets. In Supplementary Fig. S3, the predicted $\varepsilon^{sim}_{\{hkl\}<a_ib_ic_i>}$ vs Σ_{VM} and $\Delta I^{sim}_{\{hkl\}<a_ib_ic_i>}$ vs E_{VM} evolutions are compared for the random and experimental texture. The random and experimental texture simulation predicted $\varepsilon^{sim}_{\{hkl\}<a_ib_ic_i>}$ vs Σ_{VM} match very well, indicating that the mild texture and the grain neighborhoods of the $\{hkl\}<a_ib_ic_i>$ do not have a significant influence on the lattice strain evolutions of the subsets. The magnitudes of the predicted percentage change in intensity of the subsets however show differences. The differences are significant between {111}<2 1 1> and {111}<11 8 3> subsets during LP1, and {220}<14 5 5>, {220}<1 1 1>, {220}<6 1 1>, and {311}<3 3 2> after the 90° LPC. These differences arise from both different initial number of $\{hkl\}<a_ib_ic_i>$ grains, as well as the different grain neighborhoods that affect the contribution of elastic and plastic anisotropy to the intensity evolution. To differentiate between the roles of the initial number of grains and the grain neighborhoods, the $\Delta I^{sim}_{\{220\}<a_ib_ic_i>}$ vs E_{VM} obtained from the four experimental texture simulations (see section 3.3) are compared in Supplementary Figs. S4a–d. Focusing on the {220}<14 5 5> subset, the initial number of voxels belonging to this subset are 195, 107, 428 and 200 for Figs. S4a, S4b, S4c and S4d, respectively. The role of initial number of grains on the evolution of $\Delta I^{sim}_{\{220\}<14\ 5\ 5>}$ vs E_{VM} is immediately clear from the comparison of Figs. S4b and S4c where the $\Delta I^{sim}_{\{220\}<14\ 5\ 5>}$ is 1430% and 350%, respectively, at the end of the 90° LPC. The role of the grain neighborhoods is revealed when the $\Delta I^{sim}_{\{220\}<14\ 5\ 5>}$ in Figs. S4a and S4d are compared. At the end of the 90° LPC, $\Delta I^{sim}_{\{220\}<14\ 5\ 5>}$ increases by 1050% and 900%, for the 195 and 200 initial number of voxels, respectively. These significant differences highlight the need for performing crystal plasticity simulations using the exact experimental microstructures obtained from 3D non-destructive characterization techniques such as 3D X-ray diffraction. Performing crystal plasticity simulations using the experimental texture but without the experimental grain morphology will not be sufficient to predict the exact local response. Nevertheless, these results can be used to gain a qualitative understanding of the local material response. Since the texture of our 316L stainless steel is mild, performing simulations using a random texture or the experimental texture leads to the same qualitative conclusions.

5.3. Role of elastic anisotropy, plastic slip and grain neighborhood on lattice strain evolution

During any type of loading, the evolution of all $\varepsilon_{\{hkl\}<a_ib_ic_i>}$, and consequently $\varepsilon_{\{hkl\}}$, is affected by the interplay between elastic anisotropy, plastic slip and grain neighborhood effects. In the following, the contribution of these factors on the lattice strain evolution is deconvoluted and studied. We follow the approach proposed in (Upadhyay et al., 2016, 2017a) to deconvolute these effects.

The visualization of the changes in lattice strain evolution can be facilitated by plotting the polycrystalline directional elastic compliance along $\vec{g}$, i.e. $s_{\{hkl\}<a_ib_ic_i>} = \frac{\varepsilon_{\{hkl\}<a_ib_ic_i>}}{\Sigma_{11}}$ and $s_{\{hkl\}} = \frac{\varepsilon_{\{hkl\}}}{\Sigma_{11}}$, as a function of Σ_{VM}.

To separate the role of grain neighborhood and plastic slip from the contribution of elastic anisotropy, $s_{\{hkl\}<a_ib_ic_i>}$ can be compared with their respective single crystalline counterparts $s_{(hkl)[a_ib_ic_i]}$. Upadhyay et al. (2016) derived expressions (shown in equation (C1) and (C2)) of $s_{(hkl)[a_ib_ic_i]}$ for a biaxially loaded (along direction 1 and 2) single crystal having the normal to its (*hkl*) plane parallel to direction 1 (and $\vec{g}$). These equations show that the $s_{(hkl)[a_ib_ic_i]}$ evolution depends on the biaxial stress state and the degree of elastic anisotropy of the material (316L Zener anisotropic factor = 3.77). Based on this it can be deduced that for a 316L single crystal subjected to the macroscopic stress state from the 90° LPC test, the $s_{(hkl)[a_ib_ic_i]}$ response will only be affected by the non-linear gauge stress evolution but it should be independent of the plastic activity.

Next, to appreciate the role of the degree of elastic anisotropy on the single crystal response, the anisotropic $s_{(hkl)[a_ib_ic_i]}$ can be compared with its isotropic counterpart $s^{iso}_{(hkl)[a_ib_ic_i]}$ for all subsets; under the same type of loading, the latter quantity is equal for all subsets. Following Oliver and co-workers (Oliver et al., 2004), the $s^{iso}_{(hkl)[a_ib_ic_i]}$ were computed using equation set (C2) using the single

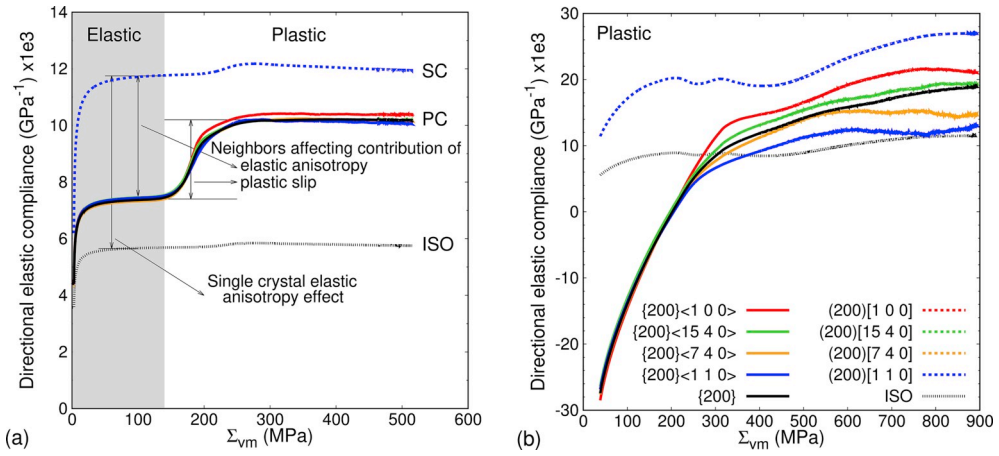

Fig. 9. Comparison between the evolutions of $s_{\{200\}<a_ib_ic_i>}$, $s_{(200)[a_ib_ic_i]}$ and $s^{iso}_{(200)[a_ib_ic_i]}$ as a function of Σ_{VM} during (a) the first loading and (b) the second loading for the 90° LPC simulation. The legend for both plots is shown in (b). The microscopic elastic and plastic regimes are highlighted. The contribution of single crystal elastic anisotropy, and the role of grain neighborhood on the contributions of elastic anisotropy and plastic slip are highlighted in (a). To facilitate the visualization of these differences, the set of directional elastic compliance evolutions for the polycrystalline (PC), and single crystal anisotropic (SC) and isotropic (ISO) cases are indicated in (a).

crystal elastic compliance components: $s_{11} = \frac{1}{E}$, $s_{11} = -\frac{\nu}{E}$ and $s_{44} = \frac{2(1+\nu)}{E}$.

Fig. 9a and b shows the $s^{iso}_{(hkl)[a_ib_ic_i]}$, $s_{(hkl)[a_ib_ic_i]}$, $s_{\{hkl\}<a_ib_ic_i>}$ and $s_{\{hkl\}}$ evolution as a function of Σ_{VM} for the {200} family during the first and second loadings of the 90° LPC; for clarity, the unloading responses are not plotted. Similar plots for the {111}, {220} and {311} families are shown in Supplementary Fig. S5. As can be expected, all the $s^{iso}_{(200)[a_ib_ic_i]}$ have the same value for a given biaxial stress ratio and they are equal to the $s^{iso}_{(hkl)[a_ib_ic_i]}$ of all the other {*hkl*} families. All the $(200)[a_ib_ic_i]$ grains have the same $s_{(200)[a_ib_ic_i]}$ values for both loadings indicating that the elastic anisotropy has the same effect on all the $(200)[a_ib_ic_i]$ single crystals. The kinks observed in the $s_{(200)[a_ib_ic_i]}$ vs Σ_{VM} and $s^{iso}_{(200)[a_ib_ic_i]}$ vs Σ_{VM} curves during both loadings are solely due to the variations in the ratio $\frac{\Sigma_{22}}{\Sigma_{11}}$ entering equation (C2); these gauge stress variations are caused by (a) the switch from equibiaxial preload (necessary to fix the cruciform samples in the machine grips) to uniaxial loading, and (b) the non-linear coupling between the cruciform gauge stresses during the macroscopic plastic regime (Fig. 2a).

To deconvolute the role of elastic anisotropy, plastic slip and grain neighborhoods to the $s_{\{hkl\}<a_ib_ic_i>}$ evolution, we need to perform the analysis in the elastic and plastic regimes. For the first loading, the range $0 \leq \Sigma_{VM} \leq 140$MPa is defined as the elastic regime and the range from $\Sigma_{VM} > 140$MPa till the end of first loading is defined as the plastic regime. After the 90° LPC however it is difficult to distinguish between the elastic and plastic regimes since none of the $s_{\{hkl\}<a_ib_ic_i>}$ remain constant for an extended period. The reasons for this could be a combination of: (i) microplasticity occurring in all the {*hkl*} families and their subsets immediately after the 90° LPC, and (ii) residual $\varepsilon_{\{hkl\}<a_ib_ic_i>}$ after the first unload along with the non-linear evolution of Σ_{11} and Σ_{22} during the second loading (Fig. 2a). Hence, with respect to the $\{hkl\}<a_ib_ic_i>$ subsets, an elastic regime is not defined during the second loading.

5.3.1. Microscopic elastic regime

For a 316L single crystal, pure uniaxial tension (such as during a dog-bone test) along the normal to one of its {200} planes results in a more compliant lattice strain response than uniaxial tension along the normal to any other {*hkl*} planes. Meanwhile, under a biaxial stress state in the 4th quadrant of the 2D stress space (see Fig. 2a), all the $s_{(hkl)[a_ib_ic_i]}$ responses are more compliant than under pure uniaxial tension (Upadhyay et al., 2016); the same is true also for the $s^{iso}_{(hkl)[a_ib_ic_i]}$ response. The combined effect of the elastic anisotropy and cruciform loading results in the $s_{(200)[a_ib_ic_i]}$ to be more than two times more compliant than $s^{iso}_{(200)[a_ib_ic_i]}$. This difference highlights the important role of single crystal elastic anisotropy on the lattice strain evolution of the {200} family and its subsets in 316L steel.

In a polycrystal, the {200} grains are surrounded by an elastically stiffer neighborhood. In order to maintain the continuity of the material under the uniaxial cruciform loading, the {200} grains will exhibit a stiffer lattice strain response and the grain neighborhood will have a more compliant response (Upadhyay et al., 2016). The grain neighborhood of each of the $\{200\}<a_ib_ic_i>$ subsets results in a nearly equal decrease (by a factor of 1.57) in their directional elastic compliances in comparison to their single crystalline counterparts.

These results imply that the role of grain neighborhood on the lattice strain evolution of the {200} family and its subsets is to decrease the contribution of elastic anisotropy by bringing the $s_{\{200\}<a_ib_ic_i>}$ response closer to $s^{iso}_{(200)[a_ib_ic_i]}$. Similar conclusions can be drawn for all the subsets of the {111} family and some of the subsets of the {220} and {311} family.

5.3.2. Microscopic plastic regime

Following the onset of plasticity during the first load, some {*hkl*} families and their subsets begin to transfer a part of their load to other families and subsets due to plastic activity. In particular, all the subsets of the {200} family begin to take more load resulting in

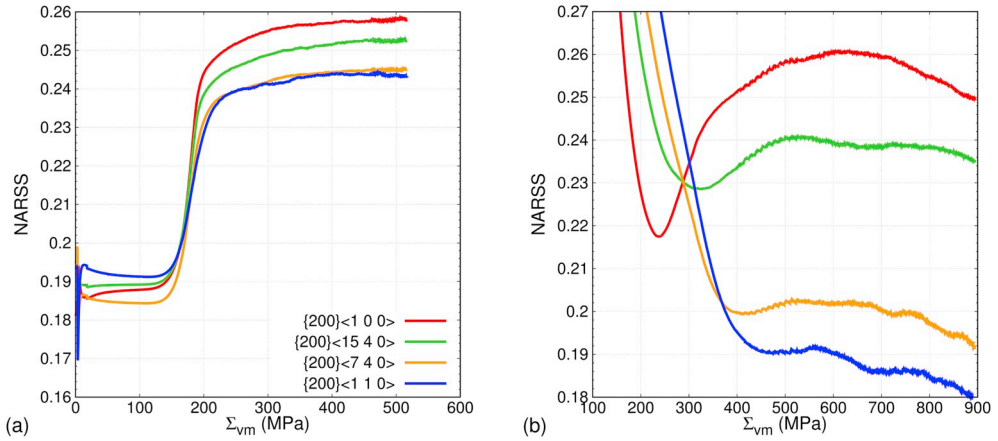

Fig. 10. NARSS as a function of Σ_{VM} for the {200}<$a_ib_ic_i$> subsets during the (a) first loading and the (b) second loading of the 90° LPC test. Due to large fluctuations in NARSS magnitudes at the beginning of second loading, the plot (b) has been cropped to start at Σ_{VM} = 100MPa. The legend for both plots is shown in (a).

an increase in their $s_{\{200\}<a_ib_ic_i>}$ (see Fig. 9a). Note that load transferring between and within {*hkl*} families can only occur in the polycrystalline case through load transfer between grains and their neighborhoods. Therefore, following the onset of plasticity, the increase in $s_{\{200\}<a_ib_ic_i>}$ is due to the grain neighborhoods which redistribute the load from those {*hkl*} families and subsets that exhibit more plastic activity to other {*hkl*} families and subsets exhibiting lower or no plastic activity.

The rate at which plastic activity occurs is determined at the slip system level of each grain in the microstructure through the shear rate per slip system. Through the viscoplastic power law relationship (equation (A6) in (Upadhyay et al., 2018)), the shear rate per slip system is dependent on the resolved shear stress τ^s and the strength of that slip system τ_c^s. The load transfer due to plastic slip activity results in changes in the τ^s of the active slip systems. These changes in τ^s are related to the changes in $\varepsilon_{\{hkl\}}$ following the onset of plasticity (Upadhyay et al., 2016). Tracking these changes in τ^s can help understand the $s_{\{hkl\}<a_ib_ic_i>}$ evolution in the plastic regime. It is however impractical to follow the slip activity on each slip system within each grain of every subset of each {*hkl*} family. Therefore, following the approach proposed in (Upadhyay et al., 2016), we first compute the average L_1-norm of τ^s averaged over all slip systems, i.e. $\frac{1}{12}\sum_s|\tau^s|$. Then, this quantity is averaged over all the voxels $N_{\{hkl\}<a_ib_ic_i>}$ belonging to an {*hkl*}<$a_ib_ic_i$> subset to give $\sum_s|\tau^s| = \frac{1}{12N_{\{hkl\}<a_ib_ic_i>}}\sum_{N_{\{hkl\}<a_ib_ic_i>}}\sum_s|\tau^s|$. Finally, $\sum_s|\tau^s|$ is normalized with respect to Σ_{VM} at each time step to get the normalized averaged RSS i.e. NARSS = $\frac{\sum_s|\tau^s|}{\Sigma_{VM}}$. Note that in this work the normalization is done with respect to Σ_{VM}, instead of Σ_{11} as done in (Upadhyay et al., 2016), to facilitate the visualization of NARSS before and after a 90° LPC. The NARSS can be considered as a generalized Schmid factor under multi-slip conditions during complex loading. The number of active slip systems and their individual τ^s eventually determine the NARSS. Therefore, it is possible that an {*hkl*}<$a_ib_ic_i$> subset has a higher τ^s on 4 of its slip systems but has a lower NARSS than another {*hkl*}<$a_ib_ic_i$> subset having slightly lower τ^s on 8 of its slip systems. Fig. 10 shows the NARSS as a function of Σ_{VM} for the {200}<$a_ib_ic_i$> subsets (a) first loading and (b) second loading of the 90° LPC.

During the elastic regime of the first loading, after the initial fluctuations due to the change from equibiaxial to uniaxial cruciform loading, all the NARSS evolve nearly uniformly. The {200}<1 1 0> and {200}<7 4 0> subsets have respectively the highest and lowest NARSS. This difference determines the average load carried by the slip systems of these subsets and is reflected in the minor differences in their respective $s_{\{200\}<a_ib_ic_i>}$ evolution. Following the onset of plasticity during the first loading, all the {200}<$a_ib_ic_i$> subsets start to take an increasing proportion of the applied load which is reflected through the increase in their respective NARSS. This increase is due to a delay in the beginning of plastic deformation in the {200} family in comparison to other {*hkl*} families resulting in a load transfer from the latter to the former.

The {200}<1 0 0> and {200}<1 1 0> subsets have respectively the steepest and gentlest increase in the NARSS. Furthermore, the slope of the NARSS vs Σ_{VM} curve of the {200}<1 1 0> subset decreases before the change in the slope of the other subsets i.e. at lower NARSS values (at Σ_{VM} = 190MPa). These changes imply that amongst the {200}<$a_ib_ic_i$> subsets, microplasticity is initiated first in the {200}<1 1 0> subset. This may result in additional load transfer from the {200}<1 1 0> subset to other subsets within the {200} family or to subsets of other {*hkl*} families. Meanwhile, the NARSS vs Σ_{VM} slope of the {200}<1 0 0> subset is the last to change implying that plasticity is delayed most in this subset. These differences in slopes combined with the differences in the onset of microplasticity in the {200}<$a_ib_ic_i$> subsets determines the increase in the magnitudes of the $s_{\{200\}<a_ib_ic_i>}$ at the end of the macroscopic elastic-plastic transition regime. Despite this increase, all $s_{\{200\}<a_ib_ic_i>}$ remain stiffer than the $s_{(200)[a_ib_ic_i]}$. This difference shows that the strong influence of the grain neighborhood on the $s_{\{200\}<a_ib_ic_i>}$ begins to decrease after the onset of plasticity in all the {200}<$a_ib_ic_i$> subsets. Following the elastic-plastic transition, the NARSS for all {200}<$a_ib_ic_i$> subsets start to gently decrease with nearly equal slopes. This implies that the entire {200} family is deforming plastically and transferring its load to other {*hkl*} families.

Immediately following the 90° LPC (Fig. 10 b), all the {200}<$a_ib_ic_i$> subsets have nearly the same NARSS value. As deformation progresses, all the NARSS decrease but with different slopes. At $\Sigma_{VM} \approx$ 220MPa, the NARSS is decreased in the following order of

subsets: {200}<1 1 0>, {200}<7 4 0>, {200}<15 4 0> and {200}<1 0 0>. After $\Sigma_{VM} \approx$ 220MPa, the NARSS of the {200}<1 0 0> subsets is the first to begin increasing again implying that load is being transferred to this subset due to relatively higher plastic activity in other {200}<$a_ib_ic_i$> subsets and possibly other {*hkl*} families. This is confirmed from the $s_{\{200\}<a_ib_ic_i>}$ evolution in Fig. 9. Meanwhile, the NARSS of the remaining three {200}<$a_ib_ic_i$> subsets keeps decreasing. Note that $s_{\{200\}<a_ib_ic_i>}$ in this stress region begins to slow down (see Fig. 9) implying that these three subsets start deforming plastically, however, the net load taken by them is still increasing. After $\Sigma_{VM} \approx$ 320MPa, the {200}<15 4 0> subset also starts to take more load, followed by the {200}<7 4 0> subset at $\Sigma_{VM} \approx$ 420MPa. From $\Sigma_{VM} \approx$ 500MPa to 600MPa, the NARSS of all {200}<$a_ib_ic_i$> subsets is nearly constant and from $\Sigma_{VM} >$ 600MPa they begin to shed their load to other {*hkl*} families resulting in the gradual decrease in the $s_{\{200\}<a_ib_ic_i>}$.

Similar analyses for the remaining {*hkl*} families show different trends in the evolutions $s^{iso}_{(hkl)[a_ib_ic_i]}$, $s_{(hkl)[a_ib_ic_i]}$ and $s_{\{hkl\}<a_ib_ic_i>}$. This implies that the elastic anisotropy, plastic slip and grain neighborhood play different roles in the lattice strain evolution of different {*hkl*} families. The results presented in this section answer question #4.

Variations in local grain neighborhoods can result in differences in the lattice strain evolution of {*hkl*} families. This can be deduced from the comparison of the simulated lattice strains using the random textured microstructure and the experimental texture microstrucure as seen in supplementary Fig. S3. It is worth noting that Kanjarla and co-workers (Kanjarla et al., 2012) reported that the effect of different grain neighborhoods is more significant for the $\varepsilon_{\{200\}}$ evolution when the polycrystal is loaded in the direction perpendicular to $\vec{g}$.

5.4. Role of elastic anisotropy and grain neighborhood on intensity evolution

Understanding the $\Delta I_{\{hkl\}}$ and $\Delta I_{\{hkl\}<a_ib_ic_i>}$ evolutions requires a different approach from the one presented above for the $\varepsilon_{\{hkl\}}$ and $\varepsilon_{\{hkl\}<a_ib_ic_i>}$ evolutions. The intensity evolutions for each {*hkl*} family occur only after the onset of plastic deformation in each of these families, pointing to the heterogeneity of the plastic activity due to the differences in the crystallographic orientations of the grains belonging to each {*hkl*} family or their subsets. The extent of plastic activity is however also influenced by the elastic anisotropy and grain neighborhood effects. In the following, the role of elastic anisotropy and grain neighborhood to $\Delta I_{\{hkl\}}$ and $\Delta I_{\{hkl\}<a_ib_ic_i>}$ are deconvoluted with the help of two new polycrystalline simulations: (i) changing only the single crystal elastic stiffness from anisotropic to isotropic, and (ii) switching the grain neighborhood of two subsets within an {*hkl*} family. The analysis is performed only for the {220} family during the first loading.

Through the first simulation, the role of single crystal elastic anisotropy on the $\Delta I_{\{220\}<a_ib_ic_i>}$ evolutions can be estimated. If the material is elastically isotropic at the single crystal level, the $\Delta I_{\{hkl\}}$ and $\Delta I_{\{hkl\}<a_ib_ic_i>}$ evolution will only be affected by the heterogeneous plastic slip activity of grains of different subsets. The isotropic single crystal elastic stiffness matrix components can be obtained using: $c_{11} = \frac{E(1-\nu)}{(1+\nu)(1-2\nu)}$, $c_{12} = \frac{E\nu}{(1+\nu)(1-2\nu)}$ and $c_{44} = \frac{(c_{11}-c_{12})}{2} = \frac{E}{2(1+\nu)}$. The macroscopic response using these isotropic components gives a response similar to the original anisotropic simulation; at the end of the second loading there is only a difference of 0.007 in E_{VM} between the two simulations. Fig. 11a shows the comparison between the $\Delta I_{\{220\}<a_ib_ic_i>}$ and $\Delta I_{\{220\}}$ obtained from the original (full line) and new simulation considering isotropy. In general, the two simulations predict similar $\Delta I_{\{220\}<a_ib_ic_i>}$ for nearly all {220}<$a_ib_ic_i$>; the largest difference occurs for the {220}<1 1 0> subset at the end of loading but it is insignificant in comparison to the $\Delta I_{\{220\}<1\,1\,0>}$ from either simulations. On average, the difference between the two $\Delta I_{\{220\}}$ is negligible. Similar results were obtained after the 90° LPC. Furthermore, other {*hkl*} families and their subsets also showed negligible differences in their $\Delta I_{\{hkl\}<a_ib_ic_i>}$ and $\Delta I_{\{hkl\}}$. These results imply that elastic anisotropy does not have a significant contribution to the intensity, and hence the texture evolution during plastic deformation for any LPC. This is in accordance with an earlier observation by Lebensohn and co-workers (Lebensohn et al., 2012) based on their EVP-FFT simulations of elastically anisotropic and isotropic polycrystals.

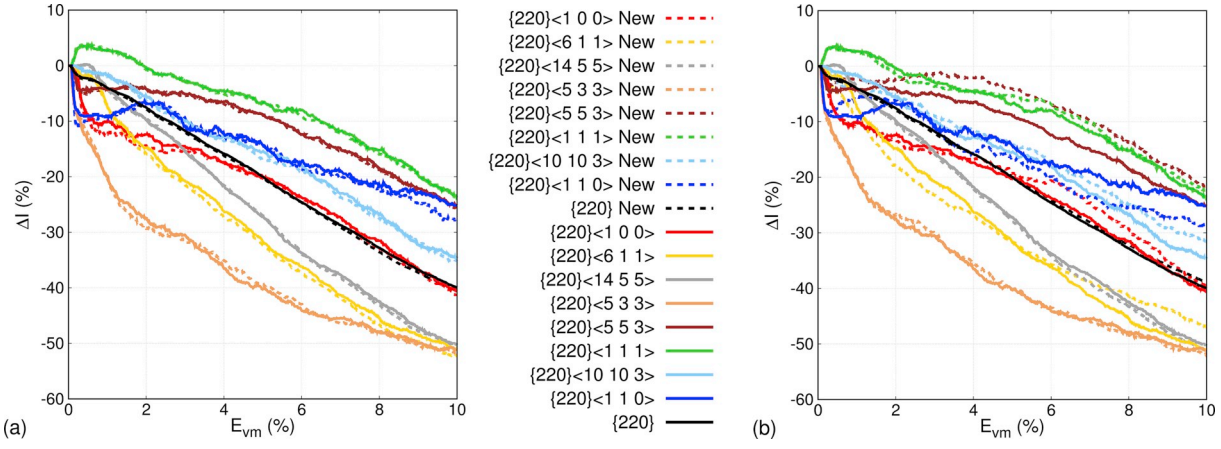

Fig. 11. Comparison between the $\Delta I_{\{hkl\}}$ vs E_{VM} evolution from the original EVP-FFT simulation for the first loading and (a) new simulation assuming an isotropic single crystal elastic response, (b) new simulation by exchanging the grains belonging to the {220}<6 1 1> subset with those belonging to the {220}<10 10 3> subset. The legend for the two plots is shown in between them.

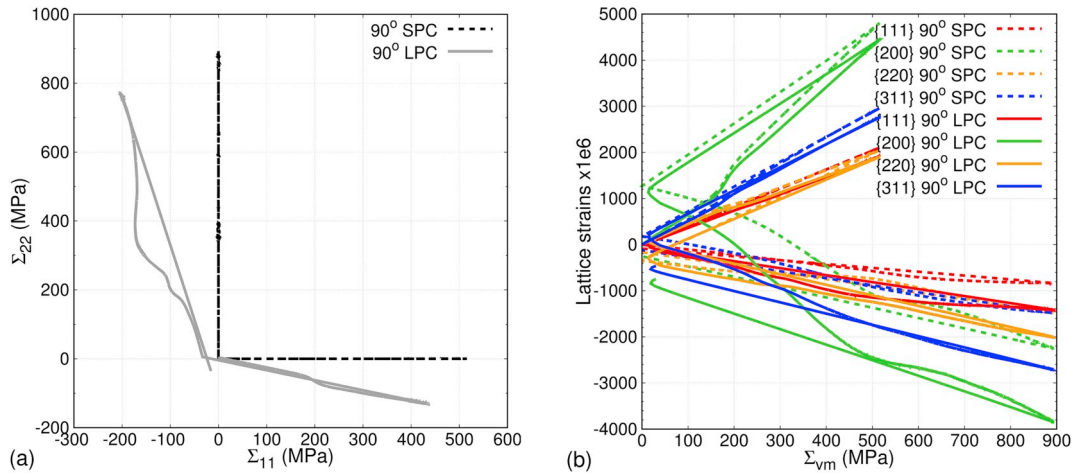

Fig. 12. Comparison between the (a) Σ_{22} vs Σ_{11} evolution, and (b) $\varepsilon_{\{hkl\}}$ vs Σ_{VM} evolution of the four $\{hkl\}$ families, during the cruciform 90° LPC and the 90° stress path change (SPC).

Through the second simulation, the role of local grain neighborhood on the $\Delta I_{\{hkl\}}$ and $\Delta I_{\{hkl\}<a_ib_ic_i>}$ evolution can be estimated. To demonstrate this, alterations are made only to the voxels of two subsets, {220}<6 1 1> and {220}<10 10 3>, belonging to the {220} family. These subsets have nearly equal number of voxels in the original microstructure, 1828 and 1767, which respectively constitute of 13.8% and 13.3% of the total voxels contributing to the {220} family. In the new microstructure, the grains that originally belonged to the {220}<6 1 1> subset are given the orientation of the {220}<10 10 3> subset and vice versa. In this manner, the grain morphology and neighborhood for these subsets and their surrounding grains are changed. The $\Delta I_{\{220\}<a_ib_ic_i>}$ and $\Delta I_{\{220\}}$ from the original and this new microstructure are shown in Fig. 11b. Switching the Euler angles of the voxels belonging to the {220}<6 1 1> and {220}<10 10 3> subsets affects not only their respective $\Delta I_{\{220\}<a_ib_ic_i>}$ but also those of other {220}<$a_ib_ic_i$> subsets. The differences between the $\Delta I_{\{220\}<a_ib_ic_i>}$ for these two simulations are more important than those occurring between the isotropic and anisotropic simulations. Furthermore, the $\Delta I_{\{hkl\}<a_ib_ic_i>}$ of $\{hkl\}<a_ib_ic_i>$ subsets from the other $\{hkl\}$ families are also affected (not shown here). Even though the differences between $\Delta I_{\{hkl\}<a_ib_ic_i>}$ evolutions from the two simulations are non-negligible, their respective average $\Delta I_{\{hkl\}}$ evolutions show very small differences. This could be because only 1.4% of the total voxels in the microstructure were changed. It can be anticipated that grain neighborhood will play an even more pronounced role in (i) hierarchical materials or (ii) materials exhibiting additional deformation mechanisms such as twinning, or transformation induced plasticity effects. The above results answer question #5.

5.5. Role of cruciform geometry on the lattice strain evolution

For 90° LPC tests performed using dog-bone samples (Gonzalez et al., 2012; Zaman et al., 2018), the angle between the stress vectors before and after the LPC is exactly 90° and during both loadings the stresses are uniaxial. However, as seen in Fig. 2a, the cruciform geometry results in a complex non-linear gauge stress evolution during the 90° LPC (Upadhyay et al., 2018) which affects the lattice strain evolution. The extent of this effect can be understood by comparing with the lattice strain evolution during a 90° LPC that results in a 90° stress path change. Fig. 12a shows the comparison between the stress evolutions predicted in the 2D space for the cruciform 90° LPC and the 90° stress path change simulations. Fig. 12b shows the comparison between their predicted $\varepsilon_{\{hkl\}}$ vs Σ_{VM} evolution for all $\{hkl\}$ families. There are noticeable differences between the respective $\varepsilon_{\{hkl\}}$ vs Σ_{VM} of these two simulations during the first loading. These differences increase significantly during the second loading. The spread in $\varepsilon_{\{hkl\}}$ vs Σ_{VM} is larger for the 90° stress path change during the first loading but significantly lower during the second loading. The kinks in the $\varepsilon_{\{hkl\}}$ vs Σ_{VM} evolution are still present indicating that this is a material response and not a consequence of the cruciform geometry. This comparison highlights the significant role that sample geometries play in determining not only the macroscopic but also the microstructural response (question #6).

6. Conclusions

An experiment-modeling synergy is used to study the lattice strain and intensity evolution of two 316L stainless steel cruciform samples subjected first to the same uniaxial loading and unloading, followed by (a) a 45° LPC or (b) a 90° LPC; the macroscopic mechanical response of these two LPCs was already presented in (Upadhyay et al., 2018). A multi-scale modeling approach is used. At the macroscale, the VPSC-FE model implemented with the crystallographic-RGBV hardening law for LPCs predicts the cruciform gauge stresses. These gauge stresses are used as macroscopic boundary conditions to drive the EVP-FFT model, implemented with the same hardening law, to predict the lattice strain evolution and variations in intensity of four $\{hkl\}$ grain families, viz. {111}, {200}, {220} and {311}. The simulated intensity variation is computed as the change in number of voxels (intragranular material points in the EVP-

FFT simulation) contributing to an {*hkl*} family during plastic deformation. The {*hkl*} families are divided into {*hkl*}<$a_i b_i c_i$> subsets on the basis of the two in-plane cruciform loading directions. The lattice strain and intensity variations of these subsets helps understand the origin of the differences between experiments and simulated predictions. They also reveal the contribution of elastic anisotropy, plastic slip, grain neighborhood and cruciform geometry on the lattice strain and intensity evolution of the {*hkl*} families. The main conclusions of this study are:

1. Simulations are able to match the experimental trends in intensity evolutions for all {*hkl*} families during both LPCs. During the first loading the magnitudes of changes in intensity are particularly well predicted for the {220} and {311} families but non-negligible differences are observed for the {111} and {200} families. These differences can be ascribed to the differences between the simulated and experimental initial 3D microstructures. Although the simulated initial microstructure well captures the overall randomness in texture of the as-received material obtained from 2D EBSD analysis, the grain neighborhood information cannot be appropriately captured from such analysis. Results reveal that grain neighborhoods have a significant contribution to the texture evolution during plastic deformation. Interestingly, after the 90° LPC, the simulations are able to predict well the magnitudes of the changes in intensity for all grain families. After the 45° LPC, simulations and experiments both reveal a negligible change in intensity due to small changes in plastic strains. To the author's knowledge, this is the first time that such a simulation-experimental comparison for changes in intensity is reported in the literature. We anticipate that such comparisons during LPC tests can help address open questions related to texture evolution during metal forming processes.
2. During the elastic-plastic transition for both loadings of the 90° LPC test, the lattice strain evolution of the {311} grain family shows significant deviations from its elastic response. This is due to the load redistribution occurring between different grain families because of the activation of heterogeneous plastic slip. However, the intensity of the {311} grains, which is representative of the texture, shows no significant changes during the entire 90° LPC. The analysis of the changes in intensity of the {311}<$a_i b_i c_i$> subsets shows that this is because a balanced number of {311} grains are rotating in and out of this family during the entire 90° LPC.
3. The simulations are able to correctly predict the lattice strain evolution, and separate and quantify the contributions from elastic anisotropy, plastic slip and grain neighborhood during LPCs. The trends of the {311} family in the plastic regime after the 90° LPC are less well reproduced. Similar to the differences in the changes in the intensity for the {200} and {111} family during the first loading, the analysis of the lattice strain evolution of {311}<$a_i b_i c_i$> subsets suggests that this could also be due to the differences between the simulated and experimental initial microstructures. A better match between the experimental and simulation results could be obtained by using a 3D microstructure input from advanced 3D characterization techniques.
4. The significant influence of the cruciform geometry induced non-linear gauge stress coupling on the lattice strain evolution was elucidated. This study also underlines the importance of the multi-scale modeling approaches, such as the one used in this work, to correctly predict the mechanical and microstructural response of engineering parts with complex geometries.
5. To understand the extent to which the material texture plays a role on lattice strain and intensity evolutions, the predictions of the random textured microstructure simulations were compared with those obtained from the microstructure simulations using the experimental texture. The mild texture of the 316L stainless steel has no significant influence on the lattice strain evolution of the {*hkl*} families and their subsets. The predicted intensity evolution of all the {*hkl*} families are also found to have similar evolutions. However, non-negligible differences were obtained between the predicted intensity evolutions of some of the {*hkl*}<$a_i b_i c_i$> subsets. Further investigation revealed that these differences were mainly due to the difference in the initial number of grains and local grain neighborhoods, and not a consequence of the mild texture of 316L stainless steel.

Acknowledgements

MVU and HVS thank the European Research Council for financial support within the ERC-advanced grant MULTIAX (339245). JC thanks the financial support from the Strategic Focus Area Advanced Manufacturing (SFA-AM) initiative of the ETH Board, Switzerland.

Appendix

A. The crystallographic-RGBV model for load path changes

The crystallographic-RGBV model (Kitayama et al., 2013; Wen et al., 2016) is used to predict the change in the critical resolved shear stress (CRSS) τ_c^s for each slip system s. The CRSS is decomposed into the contributions from dislocation accumulation/annihilation τ_d^s and back-stresses $\Delta\tau_B^s$ as follows:

$$\tau_c^s = \tau_d^s + \Delta\tau_B^s \tag{A1}$$

The dislocation accumulation/annihilation term is related to the dislocation density via the extended Taylor's law (Franciosi and Zaoui, 1982):

$$\tau_d^s = \tau_0^s + \mu b \sqrt{\sum_{s'} \alpha^{ss'} \rho^{s'}} \tag{A2}$$

where τ_0^s, μ, b, $\alpha^{ss'}$ and $\rho^{s'}$ are the initial CRSS, shear modulus, Burgers vector magnitude, interaction coefficient matrix between dislocations on slip system s and s', and the total dislocation density, respectively. The superscripts denote the slip systems s and s'.

The diagonal and off-diagonal components of $\alpha^{ss'}$ correspond to self-hardening and latent hardening coefficients, respectively. The total dislocation density is decomposed into forward ρ^s_{for} and reversible dislocation densities ρ^s_{rev}. The forward dislocation density contributes to forest hardening whereas the reversible dislocation density accounts for those dislocations that recombine (annihilate) during a reversal of shear on the slip system s. A directional sense is given to the reversible dislocation densities by splitting each slip system into s^+ and s^- according to the positive or negative Burgers vector direction (arbitrarily assigned), respectively. Consequently, the total dislocation density on slip system s is:

$$\rho^s = \rho^s_{for} + \rho^{s+}_{rev} + \rho^{s-}_{rev} \tag{A3}$$

where ρ^{s+}_{rev} and ρ^{s-}_{rev} are the reversible dislocation densities on s^+ and s^-, respectively. The total dislocation density of all slip systems is defined as $\rho = \sum_s \rho^s$.

If the slip system s^+ is activated then the shear strain increment $d\gamma^{s^+} > 0$ and $d\gamma^{s^-} = 0$. The forward and reversible dislocation density increments are computed as:

$$\begin{aligned} d\rho^s_{for} &= (1-p)\frac{d\gamma^{s^+}}{b\Lambda} - f\rho^s_{for}d\Gamma \\ d\rho^{s^+}_{rev} &= p\frac{d\gamma^{s^+}}{b\Lambda} - f\rho^{s^+}d\Gamma \\ d\rho^{s^-}_{rev} &= -\frac{1}{b\Lambda}\left(\frac{\rho^{s^-}_{rev}}{\rho^s_0}\right)^m d\gamma^{s^+} \end{aligned} \tag{A4}$$

where $d\Gamma = \sum_s |d\gamma^s|$ is the total shear increment in one grain, b is the magnitude of the Burgers vector, ρ^s_0 is the dislocation density on slip system s at the beginning of a monotonic load sequence (it is equal to the total dislocation density on slip system s immediately after a load path change), f is a fitting parameter that determines the contribution to dislocation recovery, Λ is the dislocation mean-free path, and $0 < p < 1$ is a reversibility parameter that decreases as the dislocation density increases (Wen et al., 2016). When s^- is activated, then $d\gamma^{s^-} > 0$ and $d\gamma^{s^+} = 0$ and expressions similar to (6) apply.

The back-stress coribution to the CRSS for slip system s, $\Delta\tau^s_B$, is related to the reversible dislocation densities as

$$\begin{aligned} \Delta\tau^s_B &= -\tau^s_d f^s_B\left(\frac{\rho^{s^-}_{rev}}{\rho^s}\right)^q if d\gamma^+ > 0 \\ \Delta\tau^s_B &= -\tau^s_d f^s_B\left(\frac{\rho^{s^+}_{rev}}{\rho^s}\right)^q if d\gamma^- > 0 \end{aligned} \tag{A5}$$

where f^s_B $(0 < f^s_B \leq 1)$ is a scaling factor, exponent q controls how fast the back-stress effect is nullified. Since the reversible dislocation densities increasingly recombine following a shear reversal, the contribution of back-stresses to CRSS proportionally decreases until it eventually vanishes. The crystallographic-RGBV model parameters fitted using the VPSC-FE and EVP-FFT models are reported in Table 1 in Section 3.3.

*B. Dividing the {**hkl**} families into subsets*

We use IPFs to facilitate the visualization and understanding of the procedure followed to divide the four {*hkl*} families into their {*hkl*}<$a_i b_i c_i$> subsets. Figure B1 shows the IPF for a randomly textured microstructure with 100 million grains. For an infinite number of randomly oriented grains, the IPF should be homogeneously filled with the color corresponding to value 1. However, because we use a finite number, the values slightly fluctuate around 1. The circles in the figure show the sets of grains which belong to the {111}, {200}, {220} and {311} grain families i.e. having the normals of their respective {*hkl*} planes orientated nearly parallel (within an angular tolerance of 7.5°) to the cruciform direction 1.

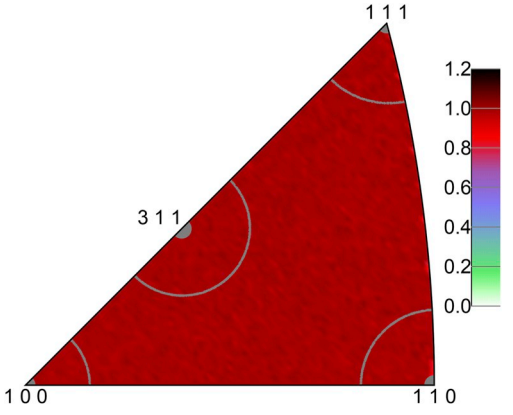

Fig. B1. IPF of a random-textured microstructure containing 100 million grains.

For the subdivision, we treat each {*hkl*} family separately. Starting with the {111} family, Fig. B2a is obtained by extracting the selected region corresponding with this family in Fig. B1. The fraction of grains in the selected region is calculated by integrating the IPF values over the selected region and dividing by the total area of the IPF triangle. It is found that only 3.4 million of the 100 million grains belong to this family, and hence the IPF area fraction occupied by the {111} family is 0.034. Similarly, the IPF area fractions of the {200}, {220} and {311} grain families are 0.026, 0.051 and 0.103, respectively.

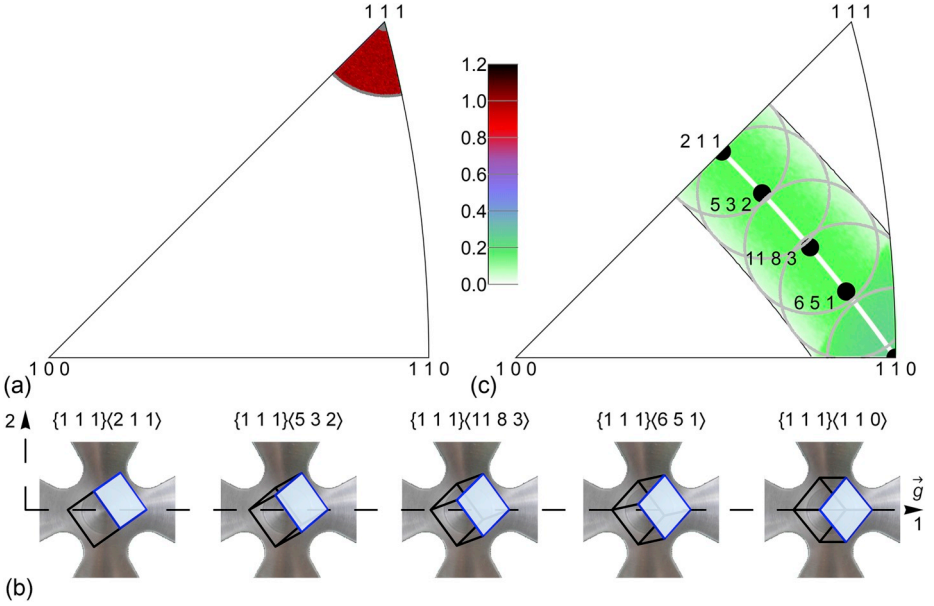

Fig. B2. (a) IPF of the {111} family when viewed along cruciform direction 1. (b) Visualization of the grain rotation about $\vec{g}$ within the {111} family, one side is highlighted for clarity. The different directions in the {111} grains parallel to cruciform direction 2 are shown. (c) The IPF of the {111} family with the possible subsets when viewed along cruciform direction 2.

For a grain to contribute to the {111} family, it must have a {111}-type plane with its normal parallel to the cruciform direction 1 (and $\vec{g}$). The grains belonging to the {111} family can have any orientation about the cruciform direction 1 (and $\vec{g}$). These orientations can be identified by looking along the cruciform direction 2. A select few of these directions for the {111} family are shown in Fig. B2b with the help of a single crystal unit cell having its [111] direction aligned along cruciform direction 1. If the IPF for the {111} family is generated while looking along cruciform direction 2, then all the {111} grains shown in the IPF in Fig. B2a occupy the wider shaded region shown in Fig. B2c. The integration over the red shaded region in Fig. B2a and over the green shaded region in Fig. B2c are the same and equal to the volume fraction of the {111} family in the microstructure, i.e. 0.034. The white line in Fig. B2c corresponds to the exact orientations without the angular tolerance of 7.5° and the width of the shaded portion is determined by this angular tolerance. Fig. B2c uses the same scale as Fig. B2a which implies that the scaling within the {111} set is with respect to all the grains in the random microstructure. The orientation distribution in Fig. B2c is inhomogeneous suggesting that some {111} grains have a higher chance of occurring in a random microstructure than others.

The {111}$<a_i b_i c_i>$ subsets are selected on the basis of the $<a_i b_i c_i>$ directions belonging to that {111} plane and falling on the white line shown in Fig. B2c. The number of grains belonging to each of these subsets depends on the angular tolerance along direction 2. This tolerance can be given any value but for simplicity it is taken to be the same as the detector angular tolerance about direction 1 i.e. 7.5°. This tolerance however creates significant overlap in the number of grains belonging to each {111}$<a_i b_i c_i>$ subset as seen in Fig. B2c. Therefore, we select only those {111}$<a_i b_i c_i>$ subsets which minimize this overlap, maximize the number of grains mapped from the {111} family, and have as low magnitudes as possible for the $a_i b_i c_i$ indices. In cases where it is difficult to achieve an optimal trade-off, the regions of some subsets are reduced in size to avoid any overlap. For the {111} family, this results in only 3 subsets as shown in Fig. 5a. The same procedure is also used to select the subsets of the {200}, {220} and {311} families as shown in Fig. 5b–d. Supplementary Figs. S6a–d shows the IPF for all {*hkl*} families along with the subsets studied and the distribution of grains in a random texture with 100 million grains.

C. Directional elastic compliance for single crystals subjected to biaxial loading

The expression for the single crystal directional elastic compliance during a general biaxial loading with the diffraction vector aligned with sample direction 1 is given as (Upadhyay et al., 2016):

$$s_{(hkl)[a_i b_i c_i]} = \frac{\varepsilon_{(hkl)[a_i b_i c_i]}}{\Sigma_{11}} = s_{11} + \frac{\Sigma_{22}}{\Sigma_{11}} s_{12} + \left(s_{11} - s_{12} - \frac{s_{44}}{2}\right)\left[\frac{\Sigma_{22}}{\Sigma_{11}}(u_1^2 u_2^2 + v_1^2 v_2^2 + w_1^2 w_2^2) - 2(u_1^2 v_1^2 + u_1^2 w_1^2 + v_1^2 w_1^2)\right] \tag{C1}$$

where s_{11}, s_{12} and s_{44} are the independent components of the single crystal elastic compliance for a cubic material, (u_1 v_1 w_1) and

$(u_2\ v_2\ w_2)$ are unit vectors parallel to the sample directions 1 (also normal to one of the $\{hkl\}$ planes) and 2 (also parallel to one of the $<a_i b_i c_i>$ directions), respectively.

Consider the case of four different single crystals having their (111), (200), (220) and (311) planes, respectively, parallel to direction 1 as well as $\vec{g}$. Their respective $s_{(hkl)[a_i b_i c_i]}$ along this direction can be deduced from equation (C1) to give:

$$\begin{aligned}
s_{(111)[a_i b_i c_i]} &= s_{11} + \frac{\Sigma_{22}}{\Sigma_{11}} s_{12} + \frac{1}{3}\left(s_{11} - s_{12} - \frac{s_{44}}{2}\right)\left[\frac{\Sigma_{22}}{\Sigma_{11}} - 2\right] \\
s_{(200)[a_i b_i c_i]} &= s_{11} + \frac{\Sigma_{22}}{\Sigma_{11}} s_{12} \\
s_{(220)[a_i b_i c_i]} &= s_{11} + \frac{\Sigma_{22}}{\Sigma_{11}} s_{12} + \frac{1}{2}\left(s_{11} - s_{12} - \frac{s_{44}}{2}\right)\left[\frac{\Sigma_{22}}{\Sigma_{11}}(1 - w_2^2) - 1\right] \\
s_{(311)[a_i b_i c_i]} &= s_{11} + \frac{\Sigma_{22}}{\Sigma_{11}} s_{12} + \frac{1}{11}\left(s_{11} - s_{12} - \frac{s_{44}}{2}\right)\left[\frac{\Sigma_{22}}{\Sigma_{11}}(8u_2^2 + 1) - \frac{38}{11}\right]
\end{aligned} \tag{C2}$$

Appendix A. Supplementary data

Supplementary data to this article can be found online at https://doi.org/10.1016/j.ijplas.2019.06.006.

References

Arnold, O., Bilheux, J.C., Borreguero, J.M., Buts, A., Campbell, S.I., Chapon, L., Doucet, M., Draper, N., Ferraz Leal, R., Gigg, M.A., Lynch, V.E., Markvardsen, A., Mikkelson, D.J., Mikkelson, R.L., Miller, R., Palmen, K., Parker, P., Passos, G., Perring, T.G., Peterson, P.F., Ren, S., Reuter, M.A., Savici, A.T., Taylor, J.W., Taylor, R.J., Tolchenov, R., Zhou, W., Zikovsky, J., 2014. Mantid—data analysis and visualization package for neutron scattering and SR experiments. Nucl. Instrum. Methods Phys. Res. Sect. Accel. Spectrometers Detect. Assoc. Equip. 764, 156–166. https://doi.org/10.1016/j.nima.2014.07.029.

Beyerlein, I.J., Tomé, C.N., 2007. Modeling transients in the mechanical response of copper due to strain path changes. Int. J. Plast. 23, 640–664. https://doi.org/10.1016/j.ijplas.2006.08.001.

Bonnand, V., Chaboche, J.L., Gomez, P., Kanouté, P., Pacou, D., 2011. Investigation of multiaxial fatigue in the context of turboengine disc applications. Int. J. Fatigue, Multiaxial Fatigue Models 33, 1006–1016. https://doi.org/10.1016/j.ijfatigue.2010.12.018.

Chen, B., Hu, J.N., Wang, Y.Q., Zhang, S.Y., Van Petegem, S., Cocks, A.C.F., Smith, D.J., Flewitt, P.E.J., 2015. Role of the misfit stress between grains in the Bauschinger effect for a polycrystalline material. Acta Mater. 85, 229–242. https://doi.org/10.1016/j.actamat.2014.11.021.

Christodoulou, N., Woo, O.T., MacEwen, S.R., 1986. Effect of stress reversals on the work hardening behaviour of polycrystalline copper. Acta Metall. 34, 1553–1562. https://doi.org/10.1016/0001-6160(86)90100-8.

Clausen, B., 1997. Characterization of Polycrystal Deformation by Numerical Modelling and Neutron Diffraction Measurements. Technical University of Denmark and Risoe National Laboratory, Denmark.

Clausen, B., Lorentzen, T., Bourke, M.A.M., Daymond, M.R., 1999. Lattice strain evolution during uniaxial tensile loading of stainless steel. Mater. Sci. Eng. A 259, 17–24. https://doi.org/10.1016/S0921-5093(98)00878-8.

Clausen, B., Lorentzen, T., Leffers, T., 1998. Self-consistent modelling of the plastic deformation of f.c.c. polycrystals and its implications for diffraction measurements of internal stresses. Acta Mater. 46, 3087–3098. https://doi.org/10.1016/S1359-6454(98)00014-7.

Collins, D.M., Erinosho, T., Dunne, F.P.E., Todd, R.I., Connolley, T., Mostafavi, M., Kupfer, H., Wilkinson, A.J., 2017. A synchrotron X-ray diffraction study of non-proportional strain-path effects. Acta Mater. 124, 290–304. https://doi.org/10.1016/j.actamat.2016.11.011.

Collins, D.M., Mostafavi, M., Todd, R.I., Connolley, T., Wilkinson, A.J., 2015. A synchrotron X-ray diffraction study of in situ biaxial deformation. Acta Mater. 90, 46–58. https://doi.org/10.1016/j.actamat.2015.02.009.

Dawson, P.R., Boyce, D.E., Rogge, R.B., 2005. Correlation of diffraction peak broadening to crystal strengthening in finite element simulations. Mater. Sci. Eng. A, Measurement and Interpretation of Internal/Residual Stresses 399, 13–25. https://doi.org/10.1016/j.msea.2005.02.029.

Deng, N., Kuwabara, T., Korkolis, Y.P., 2015. Cruciform specimen design and verification for constitutive identification of anisotropic sheets. Exp. Mech. 55, 1005–1022. https://doi.org/10.1007/s11340-015-9999-y.

Foecke, T., Iadicola, M.A., Lin, A., Banovic, S.W., 2007. A method for direct measurement of multiaxial stress-strain curves in sheet metal. Metall. Mater. Trans. A 38, 306–313. https://doi.org/10.1007/s11661-006-9044-y.

Franciosi, P., Zaoui, A., 1982. Multislip in f.c.c. crystals a theoretical approach compared with experimental data. Acta Metall. 30, 1627–1637. https://doi.org/10.1016/0001-6160(82)90184-5.

Gonzalez, D., Kelleher, J.F., Quinta da Fonseca, J., Withers, P.J., 2012. Macro and intergranular stress responses of austenitic stainless steel to 90° strain path changes. Mater. Sci. Eng. A 546, 263–271. https://doi.org/10.1016/j.msea.2012.03.064.

Han, T.-S., Dawson, P.R., 2005. Lattice strain partitioning in a two-phase alloy and its redistribution upon yielding. Mater. Sci. Eng. A 405, 18–33. https://doi.org/10.1016/j.msea.2005.05.095.

Hoferlin, E., Van Bael, A., Van Houtte, P., Steyaert, G., De Maré, C., 1998. Biaxial tests on cruciform specimens for the validation of crystallographic yield loci. J. Mater. Process. Technol. 80– 81, 545–550. https://doi.org/10.1016/S0924-0136(98)00123-X.

Hu, J., Chen, B., Smith, D.J., Flewitt, P.E.J., Cocks, A.C.F., 2016. On the evaluation of the Bauschinger effect in an austenitic stainless steel—the role of multi-scale residual stresses. Int. J. Plast. 84, 203–223. https://doi.org/10.1016/j.ijplas.2016.05.009.

Iadicola, M.A., Creuziger, A.A., Foecke, T., 2014. Advanced biaxial cruciform testing at the NIST center for automotive lightweighting. In: Rossi, M., Sasso, M., Connesson, N., Singh, R., DeWald, A., Backman, D., Gloeckner, P. (Eds.), Residual Stress, Thermomechanics & Infrared Imaging, Hybrid Techniques and Inverse Problems, Volume 8: Proceedings of the 2013 Annual Conference on Experimental and Applied Mechanics. Springer International Publishing, Cham, pp. 277–285.

Iadicola, M.A., Foecke, T., Banovic, S.W., 2008. Experimental observations of evolving yield loci in biaxially strained AA5754-O. Int. J. Plast. 24, 2084–2101. https://doi.org/10.1016/j.ijplas.2008.03.003.

Kanjarla, A.K., Lebensohn, R.A., Balogh, L., Tomé, C.N., 2012. Study of internal lattice strain distributions in stainless steel using a full-field elasto-viscoplastic formulation based on fast Fourier transforms. Acta Mater. 60, 3094–3106. https://doi.org/10.1016/j.actamat.2012.02.014.

Kitayama, K., Tomé, C.N., Rauch, E.F., Gracio, J.J., Barlat, F., 2013. A crystallographic dislocation model for describing hardening of polycrystals during strain path changes. Application to low carbon steels. Int. J. Plast., Microstructure-based Models of Plastic Deformation 46, 54–69. https://doi.org/10.1016/j.ijplas.2012.09.004.

Kuwabara, T., 2007. Advances in experiments on metal sheets and tubes in support of constitutive modeling and forming simulations. Int. J. Plast., NUMISHEET2005 Conference 23, 385–419. https://doi.org/10.1016/j.ijplas.2006.06.003.
Lebensohn, R.A., Kanjarla, A.K., Eisenlohr, P., 2012. An elasto-viscoplastic formulation based on fast fourier transforms for the prediction of micromechanical fields in polycrystalline materials. Int. J. Plast. 32–33, 59–69.
Lebensohn, R.A., Tomé, C.N., 1993. A self-consistent anisotropic approach for the simulation of plastic deformation and texture development of polycrystals: application to zirconium alloys. Acta Metall. Mater. 41, 2611–2624. https://doi.org/10.1016/0956-7151(93)90130-K.
MacEwen, S.R., Perrin, R., Green, D., Makinde, A., Neale, K.W., 1992. An evaluation of planar biaxial deformation in H19 can-stock sheet. In: Proceedings of the 13th Risø International Symposium on Materials Science. Presented at the Modelling of Plastic Deformation and its Engineering Applications. Risø National Laboratory, Roskilde, Denmark, pp. 539–545.
Marin, T., Dawson, P.R., Gharghouri, M.A., 2012. Orientation dependence of stress distributions in polycrystals deforming elastoplastically under biaxial loadings. J. Mech. Phys. Solids 60, 921–944. https://doi.org/10.1016/j.jmps.2012.01.007.
Neil, C.J., Wollmershauser, J.A., Clausen, B., Tomé, C.N., Agnew, S.R., 2010. Modeling lattice strain evolution at finite strains and experimental verification for copper and stainless steel using in situ neutron diffraction. Int. J. Plast. 26, 1772–1791. https://doi.org/10.1016/j.ijplas.2010.03.005.
Oliver, E.C., Daymond, M.R., Withers, P.J., 2004. Interphase and intergranular stress generation in carbon steels. Acta Mater. 52, 1937–1951.
Patra, A., Tomé, C.N., 2017. Finite element simulation of gap opening between cladding tube and spacer grid in a fuel rod assembly using crystallographic models of irradiation growth and creep. Nucl. Eng. Des. 315, 155–169. https://doi.org/10.1016/j.nucengdes.2017.02.029.
Prangnell, P.B., Downes, T., Withers, P.J., Lorentzen, T., 1995. An examination of the mean stress contribution to the Bauschinger effect by neutron diffraction. Mater. Sci. Eng. A 197, 215–221. https://doi.org/10.1016/0921-5093(94)09744-5.
Rauch, E.F., Gracio, J.J., Barlat, F., 2007. Work-hardening model for polycrystalline metals under strain reversal at large strains. Acta Mater. 55, 2939–2948. https://doi.org/10.1016/j.actamat.2007.01.003.
Rauch, E.F., Gracio, J.J., Barlat, F., Vincze, G., 2011. Modelling the plastic behaviour of metals under complex loading conditions. Model. Simul. Mater. Sci. Eng. 19, 035009. https://doi.org/10.1088/0965-0393/19/3/035009.
Repper, J., Niffenegger, M., Van Petegem, S., Wagner, W., Van Swygenhoven, H., 2013. In-situ biaxial mechanical testing at the neutron time-of-flight diffractometer POLDI. Mater. Sci. Forum 768–769, 60–65. https://doi.org/10.4028/www.scientific.net/MSF.768-769.60.
Saleh, A.A., Pereloma, E.V., Clausen, B., Brown, D.W., Tomé, C.N., Gazder, A.A., 2013. On the evolution and modelling of lattice strains during the cyclic loading of TWIP steel. Acta Mater. 61, 5247–5262. https://doi.org/10.1016/j.actamat.2013.05.017.
Segurado, J., Lebensohn, R.A., LLorca, J., Tomé, C.N., 2012. Multiscale modeling of plasticity based on embedding the viscoplastic self-consistent formulation in implicit finite elements. Int. J. Plast. 28, 124–140. https://doi.org/10.1016/j.ijplas.2011.07.002.
Stuhr, U., 2005. Time-of-flight diffraction with multiple pulse overlap. Part I: the concept. Nucl. Instrum. Methods Phys. Res. Sect. Accel. Spectrometers Detect. Assoc. Equip. 545, 319–329. https://doi.org/10.1016/j.nima.2005.01.320.
Stuhr, U., Spitzer, H., Egger, J., Hofer, A., Rasmussen, P., Graf, D., Bollhalder, A., Schild, M., Bauer, G., Wagner, W., 2005. Time-of-flight diffraction with multiple frame overlap Part II: the strain scanner POLDI at PSI. Nucl. Instrum. Methods Phys. Res. Sect. Accel. Spectrometers Detect. Assoc. Equip. 545, 330–338. https://doi.org/10.1016/j.nima.2005.01.321.
Takahashi, H., Shiono, I., 1991. Backlash model for large deformation behavior of aluminum under torsional cyclic loading. Int. J. Plast. 7, 199–217. https://doi.org/10.1016/0749-6419(91)90030-3.
Tasan, C.C., Hoefnagels, J.P.M., Dekkers, E.C.A., Geers, M.G.D., 2012. Multi-axial deformation setup for microscopic testing of sheet metal to fracture. Exp. Mech. 52, 669–678. https://doi.org/10.1007/s11340-011-9532-x.
Upadhyay, M.V., Capek, J., Petegem, S.V., Lebensohn, R.A., Swygenhoven, H.V., 2017a. Intergranular strain evolution during biaxial loading: a multiscale FE-FFT approach. JOM 69, 839–847. https://doi.org/10.1007/s11837-017-2299-5.
Upadhyay, M.V., Panzner, T., Petegem, S.V., Swygenhoven, H.V., 2017b. Stresses and strains in cruciform samples deformed in tension. Exp. Mech. 57, 905–920. https://doi.org/10.1007/s11340-017-0270-6.
Upadhyay, M.V., Patra, A., Wen, W., Panzner, T., Van Petegem, S., Tomé, C.N., Lebensohn, R.A., Van Swygenhoven, H., 2018. Mechanical response of stainless steel subjected to biaxial load path changes: cruciform experiments and multi-scale modeling. Int. J. Plast. 108, 144–168. https://doi.org/10.1016/j.ijplas.2018.05.003.
Upadhyay, M.V., Van Petegem, S., Panzner, T., Lebensohn, R.A., Van Swygenhoven, H., 2016. Study of lattice strain evolution during biaxial deformation of stainless steel using a finite element and fast Fourier transform based multi-scale approach. Acta Mater. 118, 28–43. https://doi.org/10.1016/j.actamat.2016.07.028.
Van Petegem, S., Wagner, J., Panzner, T., Upadhyay, M.V., Trang, T.T.T., Van Swygenhoven, H., 2016. In-situ neutron diffraction during biaxial deformation. Acta Mater. 105, 404–416. https://doi.org/10.1016/j.actamat.2015.12.015.
Wang, H., Capolungo, L., Clausen, B., Tomé, C.N., 2017. A crystal plasticity model based on transition state theory. Int. J. Plast., Special Issue on Constitutive Descriptions of Plasticity at Various Scales in memory of Prof. José J. Grácio 93, 251–268. https://doi.org/10.1016/j.ijplas.2016.05.003.
Wang, H., Clausen, B., Tomé, C.N., Wu, P.D., 2013. Studying the effect of stress relaxation and creep on lattice strain evolution of stainless steel under tension. Acta Mater. 61, 1179–1188. https://doi.org/10.1016/j.actamat.2012.10.027.
Wang, H., Wu, P.D., Tomé, C.N., Wang, J., 2012. Study of lattice strains in magnesium alloy AZ31 based on a large strain elastic-viscoplastic self-consistent polycrystal model. Int. J. Solids Struct. 49, 2155–2167. https://doi.org/10.1016/j.ijsolstr.2012.04.026.
Wen, W., Borodachenkova, M., Tomé, C.N., Vincze, G., Rauch, E.F., Barlat, F., Grácio, J.J., 2016. Mechanical behavior of low carbon steel subjected to strain path changes: experiments and modeling. Acta Mater. 111, 305–314. https://doi.org/10.1016/j.actamat.2016.03.075.
Wollmershauser, J.A., Clausen, B., Agnew, S.R., 2012. A slip system-based kinematic hardening model application to in situ neutron diffraction of cyclic deformation of austenitic stainless steel. Int. J. Fatigue 36, 181–193. https://doi.org/10.1016/j.ijfatigue.2011.07.008.
Zaman, S.B., Barlat, F., Kim, J.-H., 2018. Deformation-induced anisotropy of uniaxially prestrained steel sheets. Int. J. Solids Struct. 134, 20–29. https://doi.org/10.1016/j.ijsolstr.2017.10.029.